Elisabeth Hengge, BSc

Real-Time High-Precision Dilatometric Study of Nano-Scale Precipitation Processes during Isothermal Age-Hardening in EN AW-6060 Aluminium Alloy

Master's Thesis

to achieve the university degree of

Diplom-Ingenieurin

Master's degree programme: Advanced Materials Science

submitted to

Graz University of Technology

Supervisor

Univ.-Prof. Dipl.-Phys. Dr.rer.nat. Roland Würschum

Institute of Materials Physics

Graz, April 2018

Affidavit

I declare that I have authored this thesis independently, that I have not used other than the declared sources/resources, and that I have explicitly indicated all material which has been quoted either literally or by content from the sources used. The text document uploaded to TUGRAZonline is identical to the present master‘s thesis.

Date	Signature

Abstract

In-situ observations of the precipitation kinetics during isothermal conditions of a commercial Al-Mg-Si aluminium alloy (EN AW-6060) were conducted by high-precision dilatometry. The unique setup enables the analysis of transformations that are known to show little response in common techniques as DSC or non-isothermal dilatometry. Al-Mg-Si alloys are high-potential light alloys that are mainly used in automotive and aerospace industry. A key advantage is the adjustable hardness which is achieved by a multi-step heat treatment. In that process the microstructure is undergoing a sequence of different metastable precipitates. A variety of contradictory publications on the mechanism underlying it already exist, but isothermal dilatometry represents the perfect tool to simulate industrial processes and thus to resolve the lacking data, especially during the transformation processes.

Dilatometry was used to conduct and analyze the length response for a wide range of isothermal heat treatments from natural aging to artificial aging between 170 °C and 260 °C, up to isothermal dissolution. The measurements were supplemented by hardness tests and x-ray diffractometry, the last one providing quantitative information on the change of lattice spacing of the aluminium matrix. The results were then directly compared to theoretically obtained data of the volume change.

Calculations revealed that each of the consecutive precipitates in the aging sequence causes a change in the sign of the volume change. This enables the use of the dilatometric curves as a direct visualization of the temperature dependence of precipitate formation during isothermal aging. For instance, the formation of β'' at 210 °C causes a relative length change ($\Delta L/L_0$) of 3×10^{-5} whereas the consecutive formation of β' causes a length decrease of -4×10^{-5}. The precipitation process can be described as a sequence of continuous transitions, during which at least two precipitate-types are coexisting. The relative concentrations are thereby highly dependent on the temperature. Specific points in the dilatometric curves, as the maximum amount of β'' and β'-phase were inserted in a Time-Temperature-Precipitation diagram and extended by data extracted from literature. The apparent activation energy could be determined to be (109 ± 7) kJ/mol.

Contents

Affidavit i

Abstract iii

1 Introduction 1

2 Fundamentals 3

2.1 Nucleation and Growth of Precipitates . . . 3

2.2 Precipitation Hardening . . . 7

2.3 Aluminium Alloys . . . 9

3 Experimental Setup 13

3.1 High-Precision Laser-Dilatometer . . . 13

3.2 X-Ray Diffractometer . . . 16

3.3 Hardness Test . . . 17

4 Results 19

4.1 Chemical composition . . . 19

4.2 Dilatometry . . . 20

4.3 Supplementary Measurements . . . 30

5 Discussion 35

5.1 Precipitation Sequence in EN AW-6060 . . . 35

5.2 Precipitation Kinetics during Aging . . . 53

5.3 Dissolution Kinetics . . . 63

6 Conclusion 67

Bibliography 75

1 Introduction

Since the late 19th century, dilatometry is a well established technique for material characterization. Mainly used for investigation of phase transformations in steel and ceramics, it is best known for non-isothermal heating or cooling experiments. Application was long restricted to detecting effects that raise substantial length changes exceeding the moderate resolution of the standard equipment. As a consequence, the analysis of precipitation mechanisms in light alloys by dilatometry is a rather new field in science. For instance, publications on the precipitation behaviour of aluminium alloys studied by dilatometry was not found earlier than 2000 [1–3].

Nowadays aluminium alloys are widely used in industry due to their outstanding mechanical and electrochemical properties. The low weight per volume which - connected with high strength- enables huge possibilities in energy saving. The field of application range from automobile and aerospace to shipping industry but also building construction as well as packaging in food industry.

Among them, Al-Mg-Si alloys are one of the most promising alloys for automotive applications due to their tunable properties. During forming, the material is still soft and easy deformable, but afterwards under applying a specific heat treatment the alloying elements tend to form precipitates, which hardens the material significantly. Thereby various types of precipitates are formed, from clusters to the equilibrium phase Mg_2Si. In the industrial production processes, hardening is done during the paint baking process, where the specimen is isothermal heat treated for only several minutes up to half an hour. That is the major reason why hardness increase relay on the early-stage precipitates. Hence, detailed understanding of the precipitation mechanisms is crucial for optimizing these industrial processes.

During precipitation, these Al-Mg-Si alloys undergo a variety of nucleation, growth, dissolution, and transformation processes. Literature research reveals that up to now, details about the transition mechanisms, coexistence of precipitates, and the thermal stability of individual phases are still under discussion [4–6].

For this project, the commercial AW-6060 alloy, a low-alloyed Al-Mg-Si alloy with an Mg/Si ratio of 1.6, was chosen, mainly for one reason: It was reported that the detectable response in DSC or dilatometry is too low for reliable examination [7,8]. Because of that, the existing data is still very inconsistent. However, a new Laser-dilatometer for high-precision length measurements is now available at the Institute of Materials Physics [9], which enables precise examination of these alloys.

Dilatometry is sensitive to all microstructural changes that cause a volume and hence a length change of the sample. For investigation of precipitation kinetics, the differences in packing density of different consecutive precipitates is exploited. But there is also another competitive process contributing to the volume change, namely the impact of the magnesium and silicon atoms on the average lattice spacing of the aluminium matrix. On that account, x-ray diffraction, which was conducted to monitor the change in lattice parameter, complemented the experimental investigations.

The objective of this thesis was to clarify the precipitation mechanism in AW-6060 with focus on the transition processes and the contribution of coexisting phases. For this purpose the present work is divided into three parts. First, a detailed literature review highlights the deficiencies in the description of the precipitation sequence. This is followed by the analysis of the precipitation mechanism during natural and artificial aging using the obtained experimental data. The last part focuses on the dissolution kinetics.

2 Fundamentals

In the following two sections a short overview of the essential aspects of the nucleation and growth mechanism of precipitates as well as of the precipitation hardening will be given. For a more detailed insight the reader is referred to the textbooks by Porter and Easterling[10] and Gottstein[11].

2.1 Nucleation and Growth of Precipitates

Different types of phase transformations can occur in an alloy. Here, only one among them, the precipitation transformation which is a thermally activated diffusional transformation will be considered. For instance, this can be observed when a metal is quenched from above the solvus temperature to a temperature below. The temperature span is then denoted as the undercooling temperature. A metastable supersaturated solid solution will transform into a (more) stable solid solution with formation of stable or metastable precipitates. Depending on the material composition and the microstructure either homogeneous or heterogeneous nucleation arises. Thereby homogeneous nucleation is by far the less common mechanism. Yet, it is important for systems where coherent phases can be formed. To better understand these phenomena, a short introduction to its thermodynamics will be given.

The total free energy change (ΔG) during precipitation is composed of three terms: The interface formation energy, the misfit strain energy, and the volume free energy change (ΔG_V). The first two terms are increasing the total free energy and hence counteract the nucleation process. The volume free energy ΔG_V decreases ΔG during nucleation as the formed phase is more stable than the SSSS and therefore drives the nucleation. In Fig. 2.1 the contribution of all three terms as a function of radius of a spherical nucleus is shown. The maximum of the total free energy change (ΔG^*), as determined by the first derivative, gives the critical radius (r^*) above which a nucleus is stable.

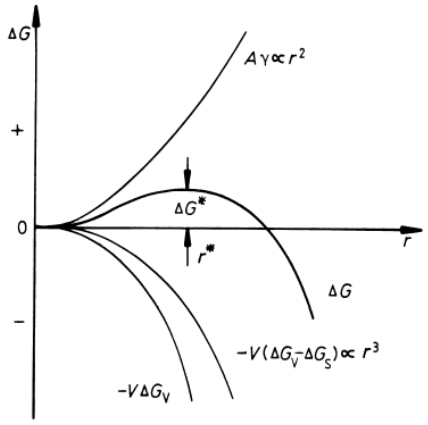

Figure 2.1: Variation of the total free energy for homogeneous nucleation. Image reprinted from Porter and Easterling[10].

The rate for homogeneous nucleation can be expressed as:

$$\dot{N}_{hom} = \omega C_0 \exp(-\frac{\Delta G_m}{kT}) \exp(-\frac{\Delta G^*}{kT}). \tag{2.1}$$

In Eq.2.1 ΔG_m denotes is the activation energy for the atomic migration per atom, C_0 the number of atoms in the precipitate (per unit volume), k the Boltzmann constant, and ω includes the vibration frequencies of the crystal as well as the area of the critical nucleus. ΔG_m and ω can be assumed to be constant for isothermal considerations but are strongly temperature-dependent with changing amount of undercooling. The Boltzmann factor $\exp(-\Delta G_m/kT)$ of atomic migration is rapidly decreasing with higher undercooling. The second exponential term describes the thermal activation for formation of stable nuclei. It remains constant until a critical undercooling (ΔT_C) is reached but afterward rises very fast. In Fig. 2.2 the influence of these two exponential terms on the nucleation rate can be seen. Nucleation first starts when ΔT_C is reached, then rises till a maximum and finally decreases again as the atomic mobility gets too small.

Apart from the considerations above, it has to be taken into account that the supersaturation decreases when the first nuclei are growing. This additionally decreases the homogeneous nucleation rate.

Most important criterion for nucleation is the minimization of the total interfacial energy. Incoherent interfaces have a far too high interfacial energy so that incoherent homogeneous nucleation would not be possible. However, some systems can form metastable coherent precipitates, such as the GP-zones in Al-Cu alloys. Their crystal structure is sufficiently similar to effectively reduce the energy barrier.

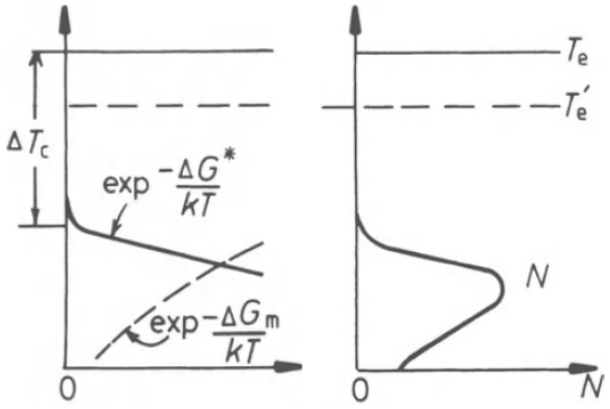

Figure 2.2: Contribution of the two exponential terms in Eq. 2.1 on the homogeneous nucleation rate. Image reprinted from Porter and Easterling[10].
T_e denotes the equilibrium solvus temperature and T_e' the reduced solvus temperature when the misfit strain energy is considered

In most systems however, the activation energy barrier for nucleation is overcome by releasing free energy when nucleation occurs at a defect site. This is then called heterogeneous nucleation as the nucleation sites are concentrated around defects, e.g., at grain boundaries. In the expression for the total energy change this results in an additional term, $-\Delta G_d$. At grain boundaries, for instance, the nucleation process can be compared to that of solidification from the melt on a substrate. The most favorable shape of a nuclei on a boundary would be that, which minimizes the interfacial energy most effectively. The energy barrier can be further reduced by nucleation on grain edges, grain corners, or at high angle grain boundaries. The latter gives the possibility that a part of the nucleus may form a coherent interface with the bulk grain. This is therefore the energetically most favorable nucleation site and nucleation will take place whenever possible. Other possible nucleation sites are dislocations. Their main contribution to reducing the energy barrier is the reduction of the lattice misfit strain energy. The interfacial energy though is not reduced by dislocations and thus they are more likely nucleation sites for semicoherent or coherent precipitates.

As soon as a stable nucleus is formed, it starts to grow. This can only be achieved when the interface is migrating into the crystal. In most cases, a precipitate show different kind of interfaces. Among them, semicoherent interfaces have the lowest mobility, incoherent ones the highest. As this results in different growth rates, the shape of the precipitate will be determined by the type of interface. The growth rate of incoherent interfaces depends on the concentration gradient at the interface and the interdiffusion coefficient (D). Eq. 2.2 represents a simplified equation for the growth rate $\nu(t)$:

$$\nu = \frac{\Delta X_0}{2(X_\beta - X_{SSSS})} \cdot \sqrt{\frac{D}{t}}. \tag{2.2}$$

Here, X_β is the mole fraction of one component in the precipitate β, X_{SSSS} the mole fraction in the super-saturated solid solution, and X_0 the mole fraction in the bulk in equilibrium after precipitation with $\Delta X_0 = X_0 - X_{SSSS}$.

Fig. 2.3 illustrates the effect of temperature and composition on ν. The precipitate growth is slow at high temperatures (low undercooling) and also at very low temperatures (high undercooling) because then the interdiffusion is too low. The maximum growth rate lies in between citePorter.

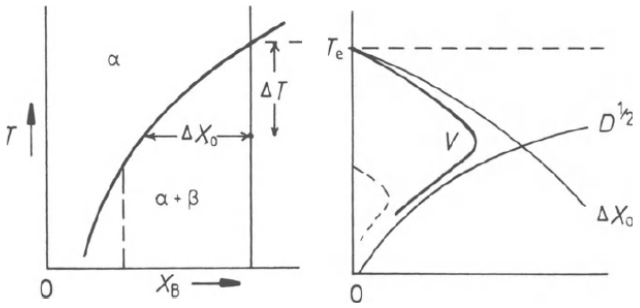

Figure 2.3: Effect of amount of undercooling on precipitate growth. Image reprinted from Porter and Easterling[10].

Arrhenius equation:

As mentioned before, precipitation is a diffusion controlled process, where higher temperatures mean faster reaction. A well established approach to calculate the activation energy by conducting temperature dependent measurements is the Arrhenius equation:

$$C = C_0 \times \exp(\frac{E_A}{kT}) \tag{2.3}$$

whereby C is a variable (e.g. could be the diffusion coefficient), C_O the corresponding pre-factor, k the Boltzmann constant and E_A the activation energy. The easiest way is to plot $1/T$ over $\log(t)$. Then the activation energy can be determined from the slope of a linear fit[11].

TTP-diagrams:

When a solid solution is cooled to lower temperature not only the equilibrium but also metastable precipitates can form. However, these precipitates are not represented in

the equilibrium phase diagram. To illustrate their precipitation behaviour so-called time-temperature-transformation- (TTT-) or time-temperature-precipitation (TTP-) diagrams are available. In a time versus temperature diagram, lines are drawn that indicate 1% and respectively 99% of transformation for a specific precipitate. Including all possible (meta-)stable phases, full information of the precipitation sequence can be extracted. Sometimes also cooling rates or other percentages of transformation are plotted additionally. When cooling rates are added, they are called Continuous Cooling Diagrams. In Fig.2.4 a schematic TTT-diagram is seen in which the phases β', β'+B' and β'' are formed inside the α-matrix. The C-shaped curves are characteristic for these kind of transformations.

They have particularly high importance in industry as they represent an easy and fast way to predict mechanical properties which result from the type and density of precipitations.[10,12]

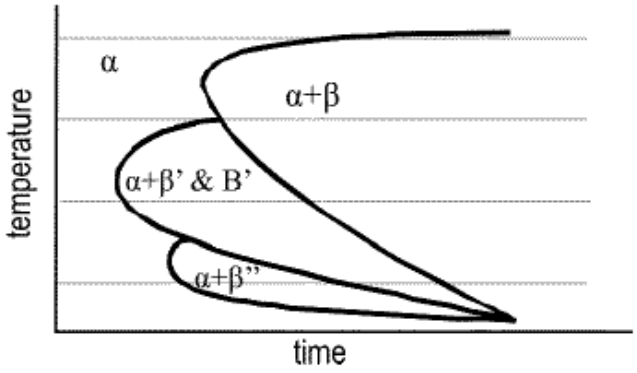

Figure 2.4: Schematic time-temperature-precipitation (TTP) diagram. Image reprinted from Milkereit et al.[12].

2.2 Precipitation Hardening

In metals, high strength is either achieved by manipulating the microstructure through mechanical deformation or by alloying additional elements and using effects as the solid solution strengthening, the dispersion hardening, or the precipitation hardening. All three mechanisms take advantage of the hindering of dislocation movement and the resultant increase in energy barrier for deformation.

Precipitation hardening occur when an alloy is cooled from a one-phase region in the phase diagram to a two-phase region. As described above, first precipitates nucleate

and then start to grow. Simultaneously, different, coexisting metastable phases can form and afterward dissolve again to form other, more stable precipitates.

Before the precipitates start to grow, mechanical effects, which at first influence the hardness, arise from the change in lattice parameter and shear modulus. Foreign atoms compress or expand the surrounding matrix which represent an attractive site for dislocations. To move forward, they have to overcome a reversing force. Furthermore, alloying results in different shear moduli compared to the matrix which also contributes to a change in total energy of dislocations.

When the precipitates grow, they first are coherent or partially semicoherent and the crystal direction of the bulk matrix proceeds through the precipitate with minor distortions. This means, dislocations can pass through the precipitate but have to overcome an additional energy barrier. Depending on the alloying elements, there are three effects which influence this barrier to varying extend.

The precipitates are sheared and the atoms above the slip plane are shifted by the length of one Burgers vector. If the formed precipitate has an ordered structure, the energy to form a antiphase-boundary has to be provided. A change in stacking fault energy from bulk to precipitate results in a different splitting width and the dislocations have to adapt to that which also costs energy. All these considerations lead to the following dependence of the stress τ_c needed for cutting the (coherent) precipitate:

$$\tau_c \propto \sqrt{r}. \tag{2.4}$$

However, it is observed that this correlation is only valid until a critical radius r_{cr}. After that, it becomes energetically more favourable for the dislocations to bypass the precipitate rather than cutting through it. The dislocation line is bending around the precipitate and anti-parallel dislocation parts are touching each other behind the particle. Thus, a free dislocation can detach from the particle and move forwards whereby a dislocation-ring is left behind around the precipitate. This mechanism is also known as the Orowan mechanism. The stress τ_{OR} for bypassing the particle decreases with r:

$$\tau_{OR} \propto \frac{1}{r}. \tag{2.5}$$

There are two other hardening mechanism, that can occur in a metal, solid solution and dispersion strengthening. But both are all included in the precipitation hardening. Solid solution strengthening occurs before any precipitate is formed and dispersion strengthening essentially is equal to the Orowan mechanism[11].

2.3 Aluminium Alloys

In the most general sense, aluminium alloys are categorized by their way of manufacturing - casting or forging. Subsequently, based on the designation of steels, one distinguishes between “cast-aluminium” or “wrought-aluminium”. This separation, however, only incorporates the mechanical properties for processing, so cast aluminium has the better mounding behaviour whereas wrought aluminium is always continuous cast and then forged. There have been a lot of different designation systems for aluminium alloys, differing from company to company or from nation to nation. The first consistent designation system was established by the North-American Aluminium Association and was later on adapted by the International Organization for Standardization (ISO). Those databases are similar and based on each other, yet not all alloys are listed in both. Nowadays, the DIN standards EN 1780 for cast aluminium and EN 573 for wrought aluminium are most widely used.

Complete designation starts with “EN”, to point out the nomenclature follows the ISO rules, then an “A” for Aluminum, followed by a “W” for wrought or “C” for cast. After a dash, finally there is a numerical series which specifies the composition. The wrought alloys are defined by a four digit system. The first number provides information about the main alloying element, the three others specify the exact alloy. The denotation of those was assigned in order of their discovery and do not refer to their composition or any property. In Tab. 2.1 the different alloying systems are listed, together with its designation and their most outstanding characteristics.

As cast-aluminium alloys are not discussed in this work, it should only be mentioned that they are classified by a five digit system (instead of four) and thereby can easily be distinguished from the wrought alloys.

Commercial alloys are defined by a nominal composition including a range of possible weight percent. This enables the overlap of compositions from one to another alloy label.

A combination of capital letters and numbers is used to clarify which additional treatment for manipulating the properties were performed. If the alloy is heat treated,

Series	Alloying Elements	heat treatable	Characteristics
1xxx	commercially pure	No	good electrical and chemical properties
2xxx	Cu (+Mg,Pb,Bi)	Yes	high strength
3xxx	Mn (+Mg)	No	"general purpose alloy"
4xxx	Si	Yes	good weldability
5xxx	Mg (+Mn)	No	high corrosion resistance
6xxx	Mg+Si	Yes	good workability and strength
7xxx	Zn (+Mg, Cu)	Yes	strongest alloys
8xxx	other	No	

Table 2.1: Designation of aluminium wrought-alloys

a "T" plus a number from 1 to 9 is added. Each number refers to a different heat treatment, among them 4 stands for solution annealed and natural aged and 6 for solution annealed and artificially aged to peak hardness[13].

2.3.1 Al-Mg-Si Alloys

In industry, Al-Mg-Si alloys are known to exhibit average to high strength, high fracture toughness, good weldability, corrosion resistance and good formability. Most of those characteristics are achieved by manipulation of the microstructure during solidification or afterward by specific designed heat treatments.

When the melt solidifies, primary precipitates, which are intermetallic phases of alloying elements or impurities, form. They are stable under normal heat treatment conditions. Secondary phases are intermetallic phases which form during heat treatments. Those precipitate are the essential particles for the precipitation hardening (see above) and enables a hardening process not until the paint baking process and after the final forming processes.

The general accepted precipitation sequence during aging consists of five distinguishable states. This number can rise up to nine, depending on amount of magnesium and silicon, the composition of other alloying elements as copper, iron or titanium, the applied heat treatment and experimental method used to investigate the precipitates.

$$SSSS \rightarrow Cluster \rightarrow ?? \rightarrow \beta'' \rightarrow \beta' \rightarrow ?? \rightarrow \beta \tag{2.6}$$

The five main precipitation stages can be generalized for all possible variations of a aluminium alloy of the 6xxx series. It starts with the supersaturated solid solution (SSSS), which forms during annealing above the solvus line. Then, after quenching,

agglomerates of solute atoms are formed. In general, those atoms do not show a specific atomic ordering and are still placed on the according substitutional lattice points as in the face-centered cubic (fcc) lattice of aluminium. Therefore they are completely coherent and show fcc crystal structure. The second well established structure is called β'' and is characterized to be the first non-fcc but still complete coherent structure. Depending on the composition, there is one intermediate precipitate, or more, between the disordered structure of clusters and the defined β'' crystal structure (denoted as "??" in the precipitation sequence 2.6). This phase is often called GP-zone (after Guinier and Preston, who first introduced them for Al-Cu alloys[14]) or pre-β'' . The crystal structure is partially or completely ordered but still differs slightly from the β'' -phase. At higher aging times, the β' phase is formed. It is characterized by being the first semi-coherent phase and often occurs simultaneously to the so called U1, U2 and B' phases. The latter ones are often also called Type A, B and C precipitates. The occurrence of those four phases (β' ,U1,U2,B') depends primarily on the amount of silicon and magnesium. Up to now, it is still impossible to predict which of them forms to what amount in one specific alloy. Finally, the thermodynamic stable precipitate is called β-phase and has the stoichiometric composition Mg_2Si. It has a fcc anti-fluorite structure and is fully incoherent[13].

Often the precipitation sequence is associated with the progress of hardness increase and decrease. Due to the high coherency, the fully coherent pre-β'' and β'' -phase is said to be the primary factor for hardness increase during isothermal aging because the strain fields induced by the precipitates interact with the dislocations The later phases, as β' and β , which start to be more and more incoherent (less pronounced strain field), show less hardening effect and are associated with the overaging regime.

Apart from the coherency strain fields, the size of the particles contribute to the hardness progress. During the whole precipitation sequence, the precipitates are continuously coarsening and growing in size. That contribution to the hardness is described in Sec. 2.2.

3 Experimental Setup

3.1 High-Precision Laser-Dilatometer

Measuring the length change response upon heating or cooling is a very common technique in industry and research to investigate macro- and microstructural phenomena. One of the best-known setups is a push-rod dilatometer, where the specimen is placed between two push-rods (in horizontal alignment) or underneath one push rod (vertical alignment), and where the length change is measured through detecting the displacement of the rod in a inductive coil. The temperature profile is usually restricted to non-isothermal heating or cooling; the resolution may be in the range of several ten nanometer.

Being interested in higher stability and/or resolution a better choice is a non-contact laser dilatometer. Here the length change is detected by means of the interference of two laser-beams, which are reflected from the specimen and a reference.

Yet, dilatometry is said to be restricted to applications where the investigated physical phenomena has a rather high impact on the overall length increase or decrease. Regarding an alloy, it may be an issue that a phase transition in a high-alloyed material is still detectable though no longer in a low-alloyed material. As a consequence, isothermal measurements, which often result in even less pronounced signals, are often not or very hard to realize in an experimental setup.

The dilatometer used in the present work has been newly developed at the Institute of Materials Physics at TU Graz. The technical description of the setup has already been published, thus the following description of the dilatometer closely follows Luckabauer et al.[9].

The setup is schematically seen in Fig. 3.1. In the description below, the denotation (A) to (J) correspond to those in the figure.

The dilatometer mainly consists of a cold wall mirror furnace (C) and a two beam laser-interferometer (B) to detect the length response. The frame (A) is made of

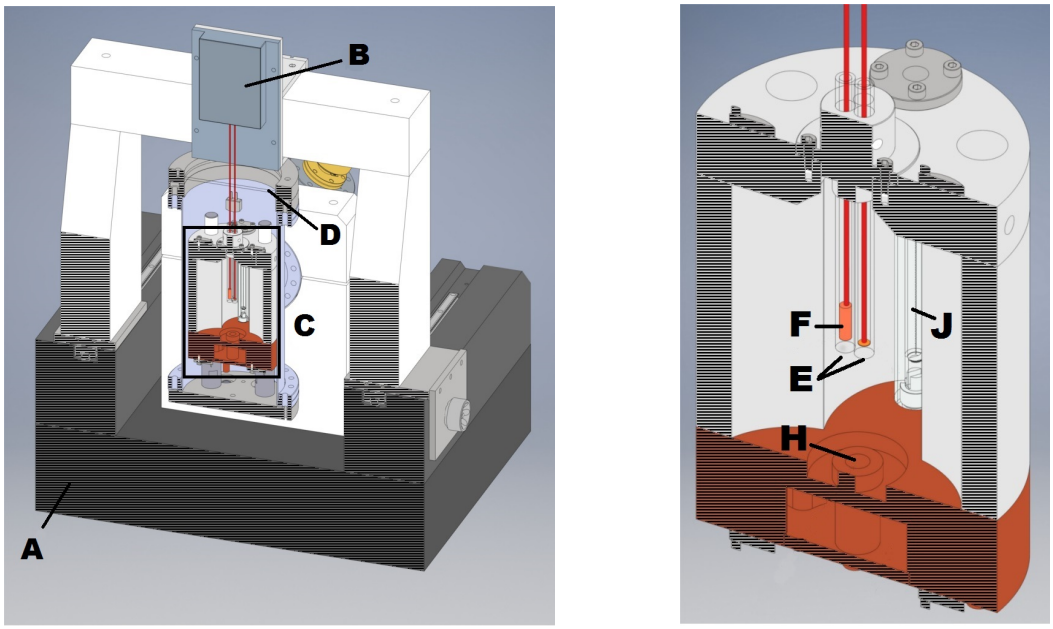

(a) Dilatometer with granite-frame **(b)** Detail view of the furnace (C)

Figure 3.1: Schematic setup of the dilatometer - Description of each part (A-J) is provided in the text.

solid granite which is mounted on a passive air suspension system. The furnace itself is placed inside a vacuum chamber supplied with a rotary vane pump and a turbo-molecular pump with which up to 4×10^{-5} mbar can be achieved.

The base of the furnace is made of three ellipsoids forming a triangle, whereby one focus of each ellipsoid is positioned in the center of the chamber. In these three central foci also the specimen holder (E) is located. Three R7s tungsten halogen lamps (J) with a length of 117 mm serve as the heating devices and are placed in the peripheral foci and surrounded by a fused silica protection tube to shield them from the vacuum chamber. Furthermore, an automatically controlled air flow is conducted through the protection tubes to stabilize the temperature of the lamps and to prevent them from overheating. The furnace is additionally temperature stabilized by a recirculating water cooling system. To be able to quench the specimen in the furnace it can be flushed with a helium flow of up to 50 l/min which is emitted centric at the bottom of the furnace (H).

A needle valve which is connected to the atmospheric pressure on one side, is additionally mounted to the vacuum chamber. With that it is possible to change the pressure in the vacuum chamber if needed.

The specimen holder (E) is a fused silica tube ranging from top of the furnace to shortly above the helium entrance. It is mounted in the central foci of one ellipsoid. Because

of the finite dimensions of the tungsten filament of the lamp, the foci are broadened and the position of the specimen is less critical than it would theoretically be expected. The cylindrical specimen with the size of 5.65 mm x 20 mm (F) is positioned on the bottom and a reflector which weighs approx. 30 g is put on top of it. The reflector is also made of fused silica with a plan parallel surface sputtered with nickel. To accurately measure the temperature of the specimen, a thermocouple is spot-welded on its surface. This was made possible by cutting a small window in the fused silica tube. A second tube and reflector is also inserted in the furnace to provide a reference surface for absolute length change measurements.

The two-beam Michelson laser-interferometer for detecting the length response is mounted on the granite frame located above the vacuum chamber. The 632.8 nm He-Ne Laser enters the chamber through a transparent glass window (D) which is also used as the loading entry. The interferometer is custom-built based on a SP120 DI manufactured by SIOS Messtechnik Ilmenau (incremental resolution of 20 pm).

Air and Helium flow as well as heating are controlled by a self-developed software. It enables isothermal as well as non-isothermal measurements superposed with a temperature modulation. The frequency of this sinusoidal modulation is restricted to the passive cooling of the system. The length response can afterward be demodulated and is then comparable with non-modulated measurements.

With this setup heating rates from 60 K/min to 600 K/min and a maximum temperature of 1100 K can be achieved. During modulated isothermal measurements the mean drift is less than 2 nm over a period of 48 hours. Over that timespan the deviations are approx. 40 nm at the highest, which consequently represents the uncertainty of the length change. Experimental varification of these data has been published by Luckabauer et al. [9].

3.1.1 Designing of argon-flow controller

For some type of measurement a defined atmospheric pressure higher than the minimum pressure achieved by the vacuum pump system, or only the rotary vane pump is necessary. For instance, the vapor pressure of some metals may be too low in the investigated temperature regime. However, passing air into the vacuum furnace through a needle valve turned out to be detrimental for the specimen as an oxide layer can form on the surface. Depending on the objective of a measurement this can affect the length response and the accuracy extensively.

Therefore, an argon flow controller was chosen to substitute the needle valve. The working range of that flow controller had to be determined accurately to ensure that it is suitable for varying the pressure inside the chamber between several and approx. 10^{-2} mbar.

This was realized by testing the throughput of the used rotary vane pump at a different, yet similar in dimensions, vacuum chamber where a argon flow controller was already installed. It turned out that a valve with a flow rate of 0-100 sccm (standard cubic centimeters per minute) is necessary for the vacuum furnace of the dilatometer.

The argon flow control valve of Bronkhorst designed for that flow rate was chosen. The functionality was checked; the achieved pressure at different mass flows can be seen in Tab. 3.1.

Table 3.1: Equilibrium pressure inside the furnace at different argon flow rates. sccm... standard cubic centimeters per minute

flow / sccm	pressure / mbar
100	2.1
50	1.6
20	1
10	0.7

3.2 X-Ray Diffractometer

X-ray diffractometry (XRD) was conducted in cooperation with the Institute of Solid State Physics. XRD provides a wide range of analytical methods for characterizing a material. One among them is the determination of the lattice constant.

The setup of the diffractometer was based on a conventional goniometer, where both the x-ray source as well as the detector is movable radial along a cycle of 240 mm radius (Theta-Theta goniometer). For operation the parallel beam mode was chosen because the covered area on the sample is larger than with a focused beam mode. The x-ray tube (40 mA, 40 kV) is emitting a Cu-Kα radiation with a wavelength of 0.154184 nm. The incident beam mask is fixed at 10 mm, the divergence slit is 1/32. On the diffracted beam side, the antiscatter-slit is 0.1 mm and the soller slits 0.02 rad. The latter reduces the divergence of the beam and enhances the parallelism. The alignment of the samples has to be done manually for this type of specimens. The aluminium plates are neither a single crystal nor a powder sample but rather has polycrystalline characteristics. Enhanced by the fact that the surface is not plane

parallel and slightly oxidized during annealing, an automated alignment would not be possible. The main purpose of aligning the sample is to achieve the best possible reflectivity of the surface. This is done by a z-, ω- and χ-scan (if needed in iteration). The first optimizes the horizontal position, the second the tilt parallel to the beam path, and the last one the tilt perpendicular to the beam.

3.2.1 Correlation of peak shift and change of lattice constant

One of the simplest ways to mathematically describe the diffraction of x-rays on a lattice is by assuming planar waves to interact with a primitive lattice. Introducing a condition for constructive and destructive interference leads to the Bragg equation

$$n\lambda = 2d_{hkl}\sin(\Theta). \tag{3.1}$$

Further geometrical considerations show that the lattice parameter of a cubic system can be calculated from the lattice distance d_{hkl}

$$a = d_{hkl}\sqrt{h^2 + k^2 + l^2}. \tag{3.2}$$

Eq. 3.1 and 3.2 enables to determine the change in lattice constant Δa (for instance, due to the precipitation of secondary phases) by measuring the shift of one specific peak ($\Delta\Theta$) over time[15].

3.3 Hardness Test

Of all possible testing methods in materials science, hardness tests belong to the easiest and fastest one and therefore are well-established for characterizing materials. There are three internationally acknowledged static hardness test procedures, the Brinell, the Vickers and the Rockwell method. All of them use a specific indenter to penetrate the material.

In the present work, the Brinell hardness test was used. Thereby the indenter is a ball of hardened steel or hard metal as tungsten carbide. The applied load will be held for a specific timespan and the formed indentation diameter will be measured. The quotient of the test force and the surface of the indentation is then defined as the hardness according to:

$$HB = \frac{0.102 \cdot 2 \cdot F}{\pi \cdot D \cdot (D - \sqrt{D^2 - d^2})} \tag{3.3}$$

with the applied force F in Newton as well as the ball diameter D and indentation diameter d. Both lengths must be given in millimeter (see Fig. 3.2).

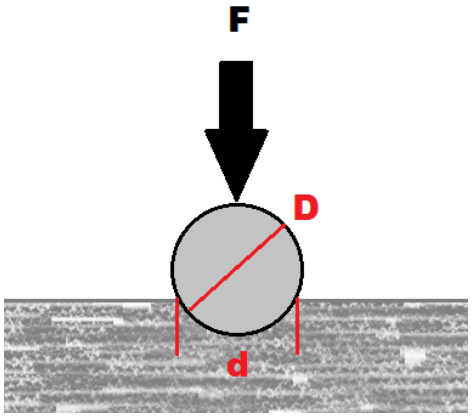

Figure 3.2: Setup of the standardized Brinell hardness test.
F / N... applied force, D / mm...ball diameter, d / mm... measured indentation diameter.

Quoting a hardness value correctly has to include the type and diameter of the indenter, the load as well as the time for indentation. For instance, 154 HBW 2.5/31.25/30 would be a complete quote of hardness measurement whereby 154 is the hardness value, HBW stands for Hardness-Brinell-Tungsten (wolfram). The diameter is 2.5 mm, the force is 31.25 kp which equals 306 N and the indentation time is 30 s. [16]

All measurements for the present work were carried out with the EMCOTEST DuraJet with a 2.5 mm tungsten indenter under 31.25 kp load. Hereafter all hardness values will only be labeled by HBW.

4 Results

4.1 Chemical composition

All specimen where prepared out of one commercially purchased Al-Si-Mg rod consisting of EN AW-6060 in T6 condition. The exact composition was determined by optical emission spectroscopy and is shown in Tab. 4.1. Based on these data a thermodynamic simulation of the equilibrium phases was done (FactSage software). The obtained results can be seen in Fig. 4.1. Both, the spectroscopy and the simulation, were performed by Prof. Pogatscher and coworkers at the Institute of Nonferrous Metallurgy at the University of Leoben.

Table 4.1: Chemical composition of the examined alloy AW-6060

Element	wt%	at%
Mg	0.58 ± 0.005	0.65 ± 0.006
Si	0.54 ± 0.006	0.54 ± 0.006
Fe	0.225 ± 0.002	0.11 ± 0.0007
Cu	0.0021 ± 0.0007	0.001 ± 0.0003
Mn	0.0049 ± 0.0001	0.0024 ± 0.0001
Ti	0.011 ± 0.0004	0.006 ± 0.0002
Zn	0.0045 ± 0.0018	0.0019 ± 0.0007

Apart from the equilibrium Mg_2Si-precipitates ("C_1"), in Fig. 4.1 three other phases i.e., $Al_{14}Fe_3Si_3$, $Ti_7Al_5Si_{14}$, and pure silicon ("Diam") have been identified in thermodynamic equilibrium. The phases containing iron and titanium are known to be primary precipitates, meaning they are formed during solidification and are stable below the solution annealing temperature of 540 °C. Pure silicon is formed in the equilibrium condition as there is not enough magnesium to bind all silicon to Mg_2Si.

For further analysis, the amount of Si and Mg available for precipitation had to be determined exactly. Assuming, that all iron and titanium is bound to the mentioned phases $Al_{14}Fe_3Si_3$ and $Ti_7Al_5Si_{14}$, the amount of Si consumed by them can be calculated.

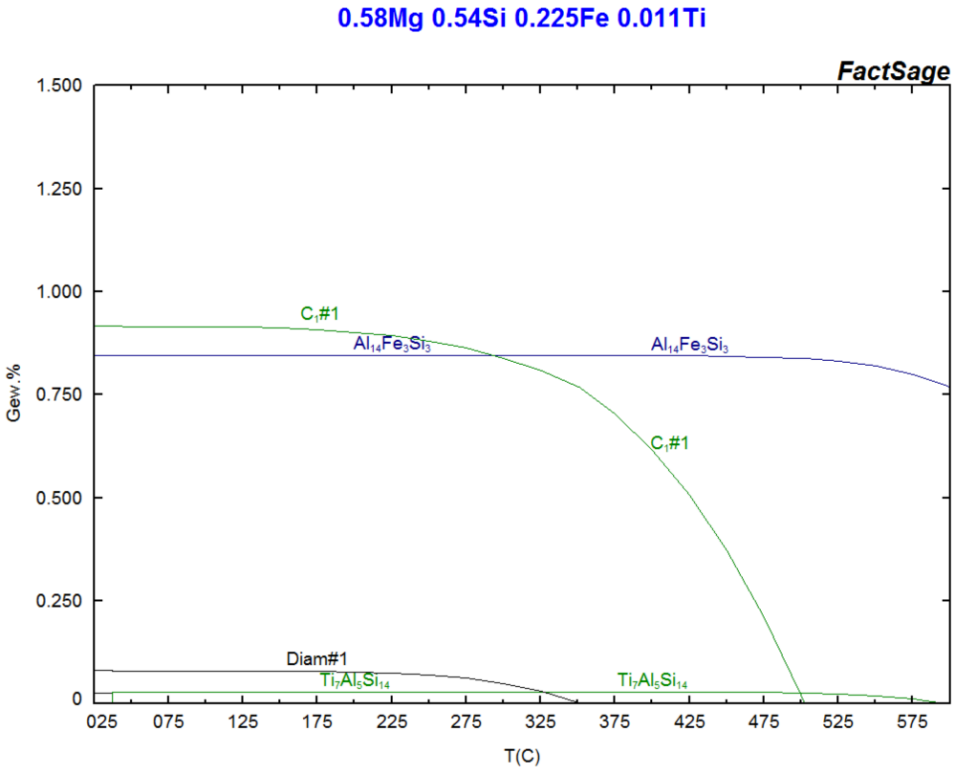

Figure 4.1: Thermodynamic simulation for equilibrium phases in AW-6060, "C_1" denotes the equilibrium Mg_2Si-phase and "Diam" pure silicon in diamond-structure.

Mg is not incorporated in any primary precipitate. The obtained concentration for Si is (0.41 ± 0.01) at% and accordingly the Mg/Si ratio is then approx. 1.6.

Please note, that only in equilibrium condition Si forms diamond-structure phases. After quenching from solid solution during formation of metastable, non-equilibrium phases this part of Si is available for precipitation.

4.2 Dilatometry

To provide optimal fitting in the specimen holder, a cylinder of 5.65 mm in diameter and 20 mm in length was machined from the initial rod. The conducted technique already provided a surface quality suitable for measuring. Then the samples were encapsulated in a glass test tube (mainly composed of Si) under argon atmosphere and annealed at 540 °C for 24 hours. The argon pressure was adjusted to be approx. 300 mbar at room temperature (RT) to ensure atmospheric pressure inside the capsule during annealing. This procedure was carried out so that all effects as grain growth and shape changes of primary precipitates can be neglected during measurements in

the dilatometer. This means that afterwards no other phenomena but exclusively the precipitation can take place.

After annealing and cleaning with acetone and isopropyl, the wires of the thermocouple were spot-welded to it and the specimen was placed inside the specimen holder. Prior to the first artificial aging period, solution annealing for 30 min was performed again, as the storage time at RT caused clustering. Solution annealing was performed under 1 mbar, artificial aging under high vacuum conditions (4×10^{-5} mbar).

The heat treatment performed always followed a procedure as seen in Fig. 4.2. It started with solution annealing at 540 °C for approx. 30 min (heating rate was either 100 °C/min or 60 °C/min) and then quenching in a helium gas stream down to RT. The gas flow was set to 25 l/min, which resulted in cooling exponentially decaying with time. As a consequence of that, quenching was stopped at 32 °C. Prior to heating to the aging temperature, the sample was kept at that temperature (so-called naturally aged) for 4 min. This timespan was necessary to start the turbomolecular pump and to evacuate the furnace.

Heating to artificial aging temperature was performed with a heating rate 100 °C/min. One measurement sequence included the whole heat treatment from start of heating to end of artificial aging. The subsequent reheating to solution annealing is part of the next measurement sequence, see Fig. 4.2. Thus, when the dissolution of the precipitate after artificial aging is discussed, a dissolution process has to be correlated to the previous measurement (e.g. dissolution detected during measurement sequence M15 corresponds to the aging process in M14).

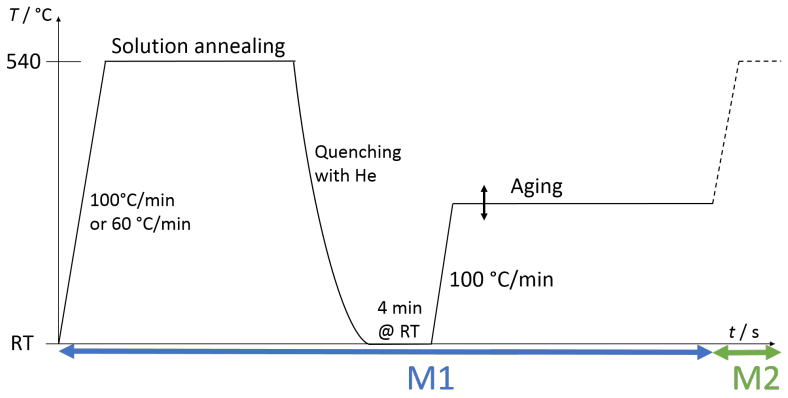

Figure 4.2: Heat treatment performed in the dilatometer.
M1... first measurement sequence, M2... subsequent measurement sequence

The objective of all measurements was to clarify the precipitation kinetics under varying heat treatment conditions. On that account, for different temperatures artificial aging

on the one hand and dissolution on the other hand were conducted. This results in many combinations of aging temperatures and timespans, whereby the dissolution was always recorded too.

The measurements were denoted chronologically starting from M01 to M40, detailed information on the heat treatments performed are shown in Tab. 4.2. For the sake of clarity the table is ranked according to the aging temperature and time. Measurements not included in this table had to be excluded due to technical problems, as thermocouples losing contact or intensity fluctuations of the laser-interferometer.

Table 4.2: Measurement series ranked according to the aging temperature. The chronological order can be derived from the label (M01-M40).

T / °C	t / s	specimen	label
30	1560000	2	M06
45	1030000	4	M40
170	26 000	2	M22
180	44 000	3	M30
	64 000	2	M12
	65 000	2	M27
	66 000	2	M16
	160 000	2	M13
	250 000	1	M02
200	61 000	2	M24
	200 000	1	M03
210	6 000	2	M17
	14 400	2	M28
	54 000	2	M19
	71 700	4	M38
	180 000	2	M14
	142 000	2	M18
	150 000	1	M01
	333 000	3	M35
220	150 000	1	M04
230	330 000	2	M25
	350 000	1	M05
240	240 000	3	M33
260	230 000	3	M31

Chronologically, the measurements were conducted in three separates sets. All together 4 different sample, from the same commercial rod, were used.

1. First set of measurements (M01-M10, specimen 1) was done with superposed temperature modulation with an amplitude of 0.6 °C and a frequency of 4 mHz

during artificial aging. The results were demodulated afterward so that they could be compared to the other measurements.

2. The second set (M11-M28, specimen 2) was then performed under isothermal conditions for various temperatures. It has to be mentioned that between the first and second set of measurements a new air cooling was mounted in the laboratory. Cooled air in now uniformly released from the ceiling and should regulate the temperature in the room with $\pm 0.3\,^{\circ}\mathrm{C}$.

3. Prior to the third set of measurements (M30-M38, specimen 3 and 4), the needle valve for regulating the pressure inside the furnace was replaced by an argon flow controller. For detailed information about the construction, see Sec. 3.1.1.

4.2.1 Choice of measurement-onset

After heating up the specimen to the aging temperature, a proper onset point to start the length change measurement had to be chosen. It turned out, that this procedure was a crucial part in analyzing the measurements because the absolute length change, which is particularly pronounced in the first few 100 seconds for some measurements, is dependent on that onset. On the other side, it is important to note that the analysis of peak positions and other characteristic points at a specific time are not much influenced by the variation of the onset point. Several approaches were tested for choosing an onset:

First, it was assumed that the heating is nearly instantaneous and there are no other influences on the length response rather than that from the specimen. The design of the dilatometer was constructed in a way that all other contributions (from the fused silica reflector etc.) should be canceled out. Moreover, it was assumed that the controlling software (based on the proportional-integral-derivative principle , so-called PID) is regulating the temperature, thus the heating of the specimen so that the transient oscillations at the start of a isothermal measurement are reproducible and more or less the same for different temperatures. According to that, the onset of each measurement could be chosen by defining a timespan after starting the heating (in dependance of the aging temperature). However, this resulted in high deviations among equivalent measurements.

The second approach was to calculate the heat transfer in a cylindrical specimen of aluminium in dependence of the real heat treatment profile applied. With that the

lagging between length response of the whole specimen and temperature response on the surface could be estimated. Yet, this difference turned out to be negligible small.

Considering the assumptions above, the question rises what else could influence the thermal equilibration of the specimen and the whole system. The quality of the contact point of the thermocouple with the specimen is hard to control and sometimes the contact is lost. However, experience shows that only a slight decrease in thermal contact results in an immediate and pronounced oscillation of the temperature regulation. This arises as the regulation is dependent on the output of the thermocouple itself. The PID-parameters are optimized for a very good contact and are very sensitive to any change in that.

During annealing air is passed inside the furnace to rise the pressure up to 1 mbar. As mentioned, this pressure is needed to hinter magnesium from evaporating. However, at that elevated temperature aluminium and also magnesium is likely to form an oxide. As it can be assumed that nevertheless magnesium is still diffusing to the surface, the formation of that oxide layer may even be enhanced compared to pure aluminium. Once formed, the oxide is a very efficient thermal insulator because the thermal conductivity is more than 10 times worse than of metallic aluminium. The oxide layer is therefore reducing the heat transfer inside the aluminium. Additionally, one has to consider that the PID-parameters were optimized once for a specimen without oxide and for one specific temperature. Diverging from that conditions the transient oscillations at the beginning may be changing. However, adjusting these parameters would be beyond the scope of this work.

At last, one has to be aware that the oxide layer may be changing when several measurements are done with one specimen. Furthermore, those measurements of specimens without any oxide have to be comparable to measurements containing a surface layer.

Combining all considerations above, a procedure to define an onset was introduced. The measured temperature profile was smoothed with the spline smoothing algorithm of MATLAB (smoothing parameter of 1×10^{-8}). All profiles then followed one of the following two pathways.

Either it is overshooting followed by undershooting and then approaching $\pm 0.01\,^{\circ}\mathrm{C}$ of the target temperature quite fast or else it is first overshooting and then approaching this threshold rather slow. In the first case, reaching $\pm 0.01\,^{\circ}\mathrm{C}$ was chosen as onset point, in the second case reaching $\pm 0.02\,^{\circ}\mathrm{C}$ has been defined as the onset. The difference in thermal expansion between these two thresholds is in the range of the

uncertainty of the dilatometer and can therefore be seen as equivalent with respect to further analysis. This procedure was subsequently applied to all measurements, both for aging and annealing.

Each of the figures 4.3 and 4.4 shows a series of measurements at 180 °C and 210 °C, respectively. The applied heat treatments are exactly the same, however, the specimens have been different, both figures include measurements of three different specimen. Both figures impressively demonstrate the excellent reproducibility of the measurements. The minor deviations at 210 °C, particularly for M35, may be due to effects arising from the evaporation of magnesium. M35 was conducted with a sample already exposed to several annealing procedures and had been replaced after this aging process at 210 °C.

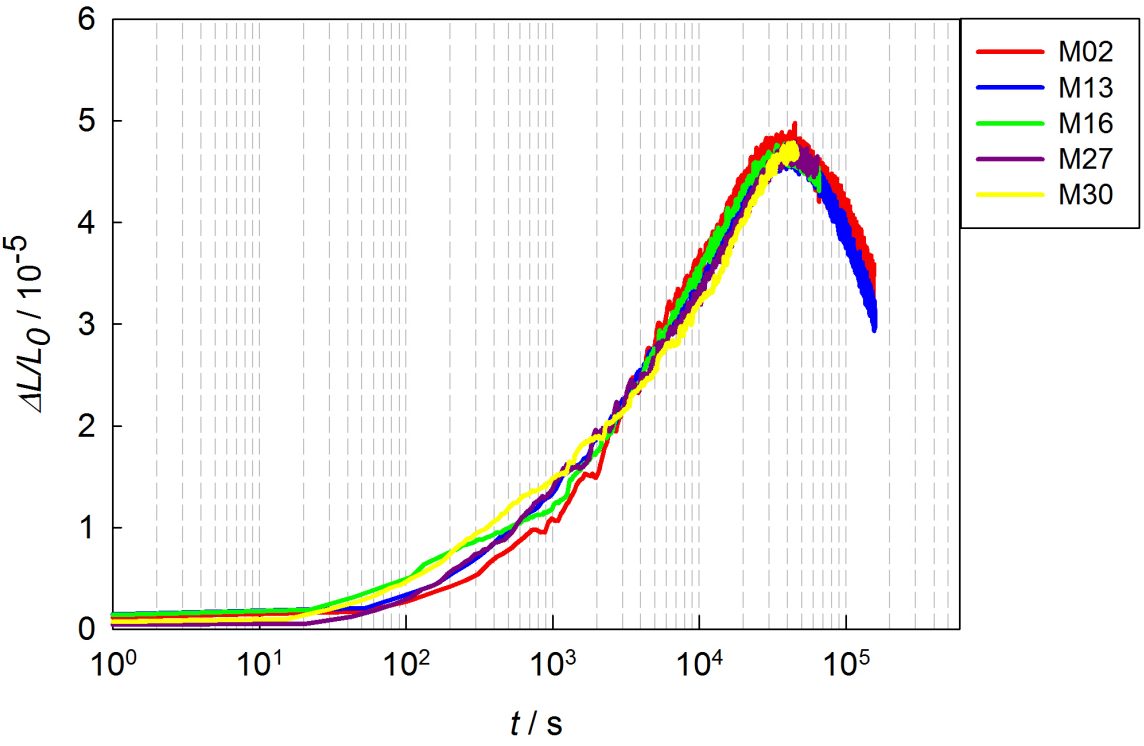

Figure 4.3: Relative length change during isothermal aging at 180 °C.

4.2.2 Artificial Aging

A comparison of the length response upon aging at different elevated temperatures, between 170 °C and 260 °C, can be seen in Fig. 4.5. At temperatures below 230 °C the length is first increasing, followed by a slow decrease. With decreasing temperature

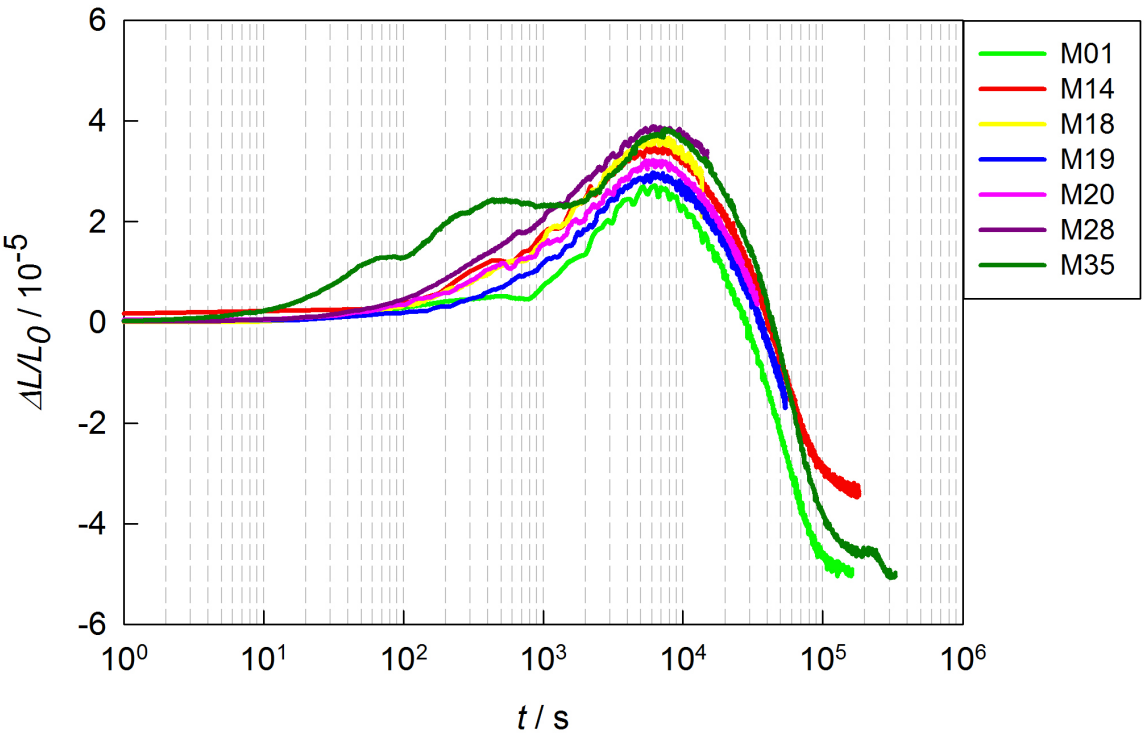

Figure 4.4: Relative length change during isothermal aging at 210 °C.

the peak in length change becomes more pronounced and is shifted to longer times. At temperatures below 200 °C the decrease is too slow to reach the minimum on a reasonable timescale.

If the isothermal aging temperature is however increased to values above 230 °C, no initial growth of the specimen can be detected at all. Instead, the length decreases rapidly until it reaches a nearly constant plateau for large annealing times. The inflection point is thereby shifted to earlier times and higher values of length reduction.

At measuring times longer than 10^5 s, as well as at the temperature of 260 °C after approx. 3×10^4 s, some minor fluctuations in the curves can be seen. They are assumed to result from small changes in the average room temperature of the laboratory. As the Laser is passing through a few centimeters of unprotected air, the interferometer also includes a room temperature sensor. Correlating the room temperature with the length change signal from the interferometer, it seems as if long term fluctuations in room temperature are influencing the signal. In Fig. 4.6 the temperature evolution in the laboratory is shown together with the length change at 210 °C (M35) after reaching the plateau at approx. 1.3×10^5 s. The plot starts at 1.5×10^5 s, which means that constant conditions regarding the length change should already have been reached.

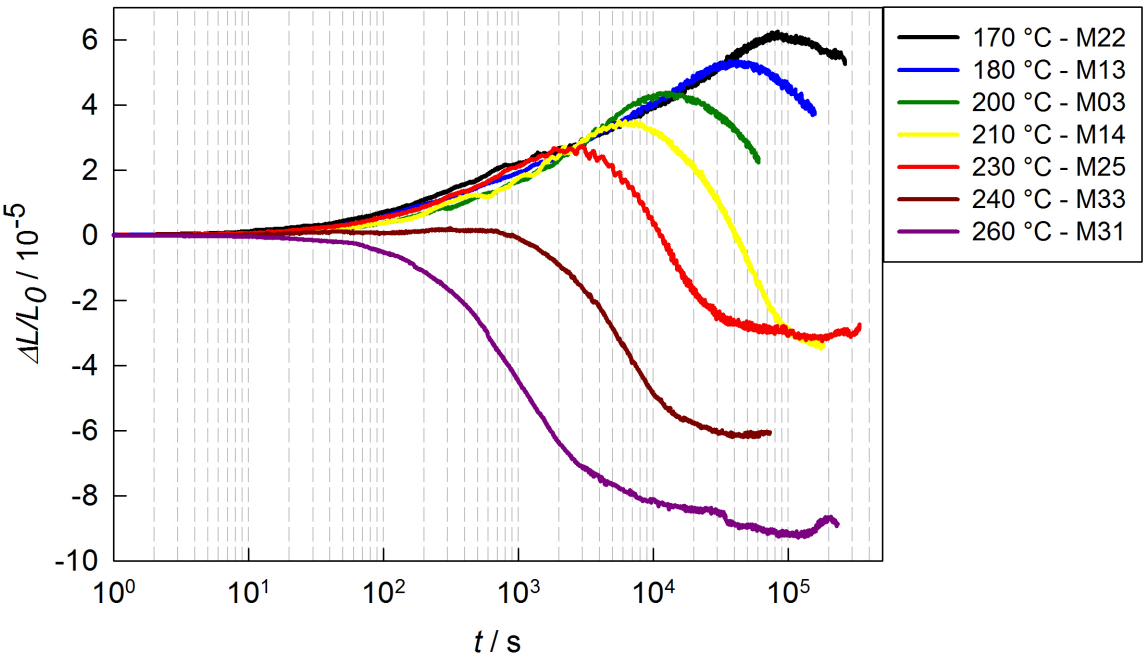

Figure 4.5: Relative length change during isothermal aging at varying temperatures.

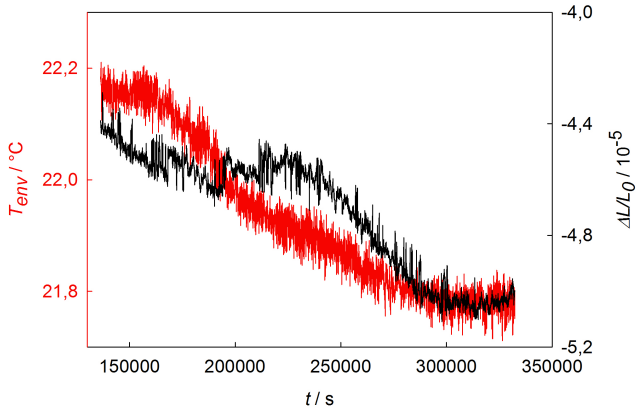

Figure 4.6: Correlation of the temperature variations in the laboratory (red) and the length response (black).

4.2.3 Natural Aging

Additionally to investigating the length response upon artificial aging, the natural aging behavior was measured. As the dilatometer do not have an active cooling device, temperatures slightly above room temperature were chosen to ease the temperature stabilization. First, aging at 30 °C and afterward at 45 °C were performed. The onset for these two measurements were defined differently because it was difficult for

the controlling software to stabilize the system at those low temperatures. Onset was defined at the time when the target temperature was passed for the first time, before overshooting. Hence, in the resulting curves the temperature oscillation at the beginning are visible too. Both curves show similar trends, although the length increase is less pronounced at 45 °C.

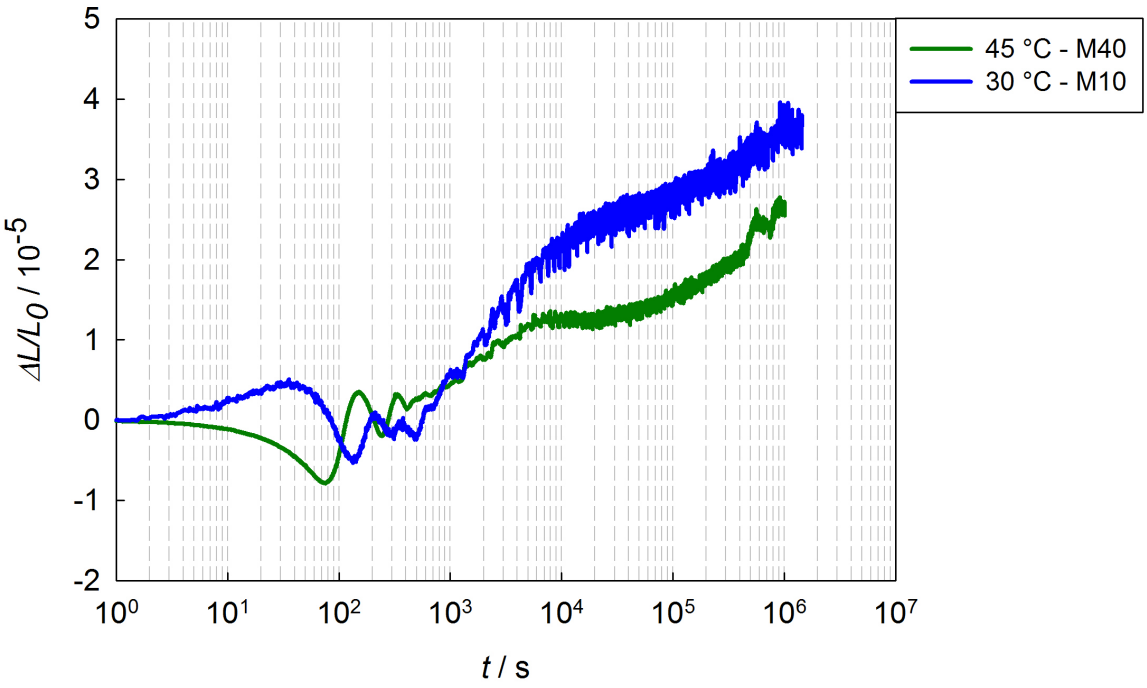

Figure 4.7: Relative length change during natural aging.

4.2.4 Solution Annealing

Subsequent to each aging of the specimen, reheating to 540 °C and dissolution of the precipitates was performed. In Fig. 4.8 a few dissolution processes together with the preceding aging at 180 °C (green and blue curve) and 210 °C (red, purple and cyan) are seen.

At first sight, the behaviour during solution annealing appears to be correlated with the preceding aging. Starting at the peak position of aging results in a length contraction (green and cyan curves). Further, starting from a point during aging where the length is already significantly decreasing, results in a slight increase or a constant length during dissolution. However, there are two aspects that have to be considered additionally.

First, the absolute length decrease during annealing should correspond with the length increase during aging. Otherwise the specimen would grow each measurement cycle.

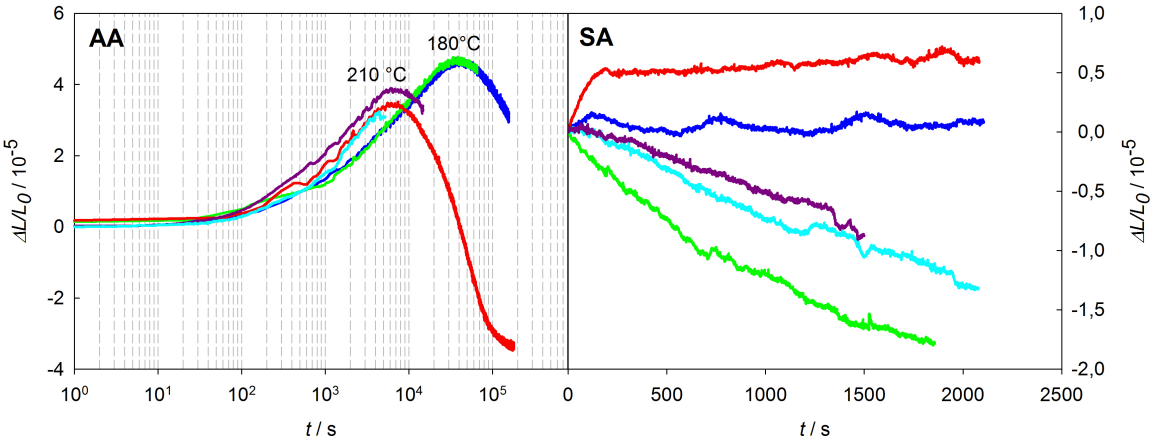

Figure 4.8: Relative length change during solution annealing at 540 ° C (SA, right) directly after artificially aging (AA, left).
green: M12 (AA) and M13 (SA) , blue: M13 (AA) and M14 (SA), cyan: M17 (AA) and M18 (SA), purple: M18 (AA) and M19 (SA), red: M14 (AA) and M15 (SA)

Clearly, this is not the case for any measurement shown. Aging for 66 000 s (green curve) results in an increase in $\Delta L/L_0$ of 4×10^{-5}. Subsequent annealing only shows a change in $\Delta L/L_0$ of 1.8×10^{-5}. Secondly, it can be assumed that aging for 14400 s at 210 °C and for 160000 s at 180 °C should result in a comparable state in the precipitation sequence and, therefore, a similar length decrease should be seen during dissolution. Though, it is clearly visible that the curves do not follow these constraints. One explanation could be that additionally to a dissolution process an oxide layer is formed during annealing. Then, the length decrease due to dissolution would be superposed by a length increase due to the formation of the oxide.

After installing an argon flow controller, which enables to pass argon inside the furnace instead of air, another set of measurements was done. Now, oxide formation should be avoided. In Fig. 4.9 two examples are shown. Although originating from completely different states in the precipitation sequence, both measurements show nearly the same behaviour. But more importantly, after removing the specimen from the dilatometer, a brownish layer was clearly visible on the inside of the fused silica tube, where the specimen was standing. X-ray fluorescence measurement (conducted by Dipl.-Ing. Stefan Pachmajer, Institute of Solid State Physics) indicated that mainly magnesium is evaporating from the specimen. The complete analysis is seen in the appendix Sec. 6.

To verify these assumptions, pictures were taken of the specimens with a scanning electron microscope. They were conducted at the Institute of Materials Science and Joining at TU Graz by Dipl.-Ing. Fatemeh Iranshahi and Dipl.-Ing. Ricardo

Buzolin. Two specimens, which have been used for dilatometric measurements, were investigated, one measured before installing the argon-flow the second afterwards. The results achieved with EDX were quite obvious as the first had a pronounced oxide layer on it. The thickness was varying greatly but reached up to a few μm. The second sample did show some oxide on the surface but the majority was oxide free. Detailed information on the SEM measurements are summarized in the appendix Sec. 6.

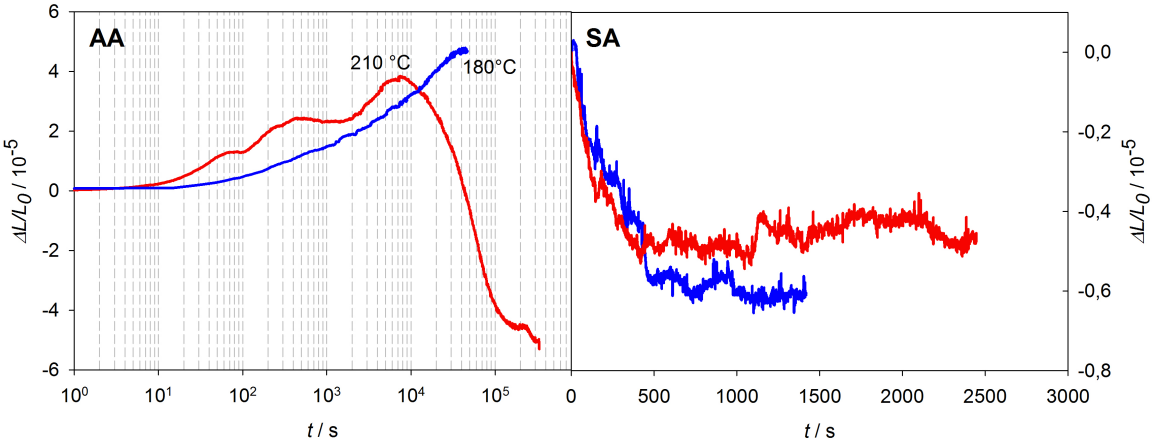

Figure 4.9: Relative length change during solution annealing at 540 ° C (SA, right) directly after artificially aging (AA, left) under Ar-atmosphere.
red: M35 (AA) and M36 (SA), blue: M30 (AA) and M31 (SA)

4.3 Supplementary Measurements

To complement the dilatometric measurements, both hardness tests and x-ray diffraction were performed. Latter was used to determine the change in lattice constant of the bulk matrix.

4.3.1 Hardness

The specimens for hardness tests were prepared by cutting 4 mm thin discs of the 10×10 mm rod. The same rod was used for all specimen used including dilatometric and XRD measurements. Cutting was performed by an automatic high precision saw to ensure plane parallel surfaces. All specimen were annealed at 540 °C for 30 min under atmospheric conditions and afterward water quenched to RT followed by natural aging for 4 min to coincide with the heat treatment done in the dilatometer. A drying furnace was used for aging at 180 °C and 210 °C and, for controlled natural aging,

at 30 °C . Hardness tests were done directly after quenching and at times equally distributed on a logarithmic time scale. For each measurement a different specimen was used and the mean value of 5 indentations was calculated. Fig. 4.10a and Fig. 4.10b feature the resulting hardness curves at 180 °C and 210 °C, Fig. 4.10c the hardness progression during natural aging (30 °C). The temporal evolution of all three curves agrees with the length change, only at 210 °C the dilatometric curve starts to rise earlier and also reaches its maximum in advance.

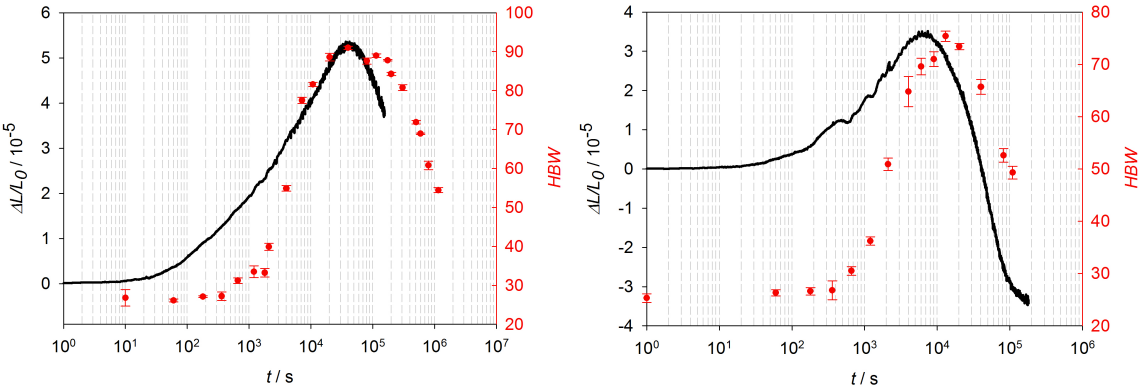

(a) 180 °C **(b)** 210 °C

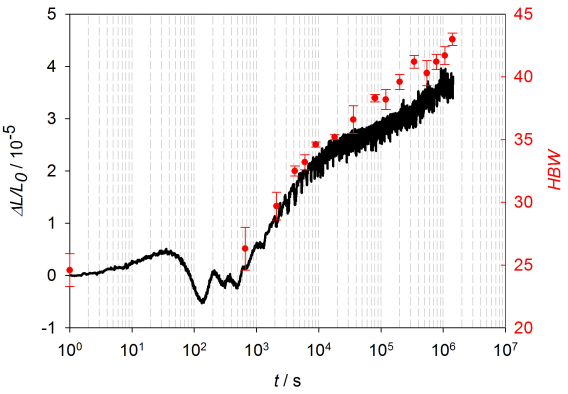

(c) 30 °C

Figure 4.10: Brinell hardness measured at ambient temperature after aging at 180 °C (a), 210 °C (b), and 30 °C (c). The relative length change is shown for comparison.

4.3.2 X-ray diffraction

The specimens for x-ray diffraction were prepared in a similar way to those for the hardness tests. However, before annealing they were ground and polished to achieve the best possible surface for diffraction experiment. Annealing was done afterwards in the tube furnace, however, under a low argon flow to reduce oxidation of the surface.

After water quenching to RT the specimens were cooled in liquid nitrogen to hinder any atomic rearrangement until they were put inside the diffractometer.

All measurements were performed by Dipl.-Ing. Stefan Pachmajer at the Institute of Solid Sate Physics with a diffractometer of type PANalytical Empyrean. After alignment (z-,ω- and χ-scan) of the first sample, an overview Theta-Theta scan was conducted (Fig. 4.11). The spectrum mainly shows the known diffraction peaks for aluminium, which are indicated in the figure by the denotation of the according lattice direction (Miller-index). The high intensity of the (200)-peak reveals a preferred direction of the grains in this direction. All other peaks belong to oxides from the surface or iron and titanium containing precipitates. Unfortunately, without further analysis, it was not possible to explicitly correlate these peaks to their origin. The penetration depth of the x-ray is approx. $1\,\mu$m, hence thin oxide layer or other contamination on the surface would not influence the measurement significantly. For determination of the lattice parameter change the (200) and (311) peaks from the aluminium were chosen for measurement. The first has the highest intensity, the second occurs at the highest angle which provides the most accurate measurement.

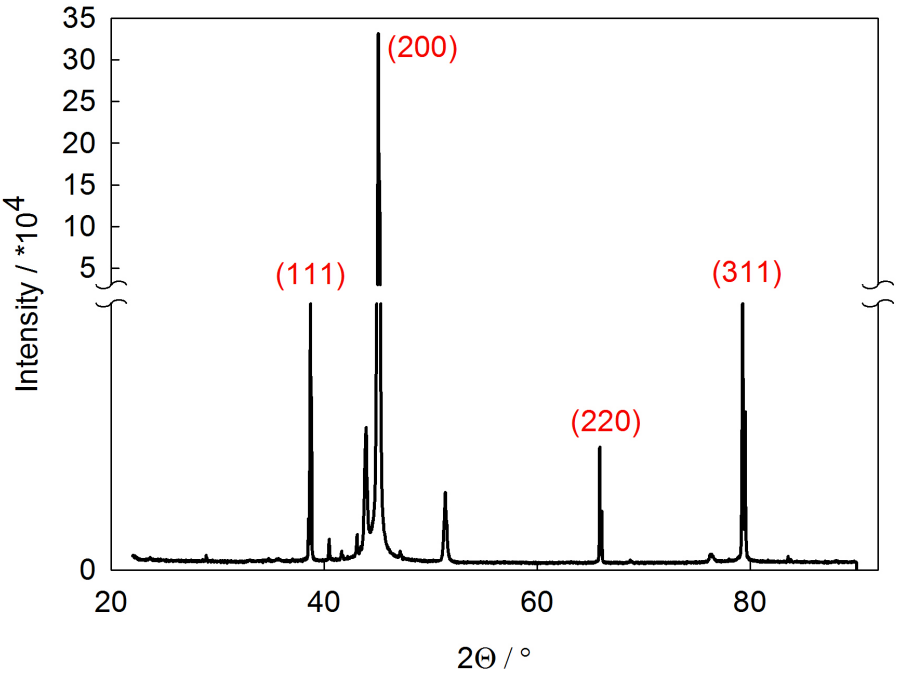

Figure 4.11: Theta-Theta Scan (so-called Gonio Scan) at RT. The Al-peaks are denoted by the Miller-indices.

For the measurements during aging a heating stage was mounted in the diffractometer. This provides the possibility to do isothermal conditions at $(180 \pm 0.2)\,°$C. After ensuring that the specimens had underwent 4 min of natural aging at RT, they were

put on the hot heating stage and alignment as well as adjusting the measurement program was conducted. This procedure took 46 min for the first and 21 min for the second measurement.

One measurement included aging for about 60 hours (approx. 220 000 s). For each point first a Z-optimization, than an ω-optimization and finally the Theta-Theta scan over the peak in a batch processing program was conducted. One iteration took 313 s and readjusting the setup additionally 90 s. This resulted in 608 for the first (311-peak) and 396 measurements points for the second (200-peak) measurement. During the second measurement, the software cut off the program after 320 iterations and was not restarted by the operator until 24 hours later .

In Fig. 4.12 the change in peak shift after 84 000 s, 166 000 s and 248 000 s of the 311-peak together with a modified-Gaussian fit as a guide for the eye is seen. The shift in the peak maximum is clearly visible.

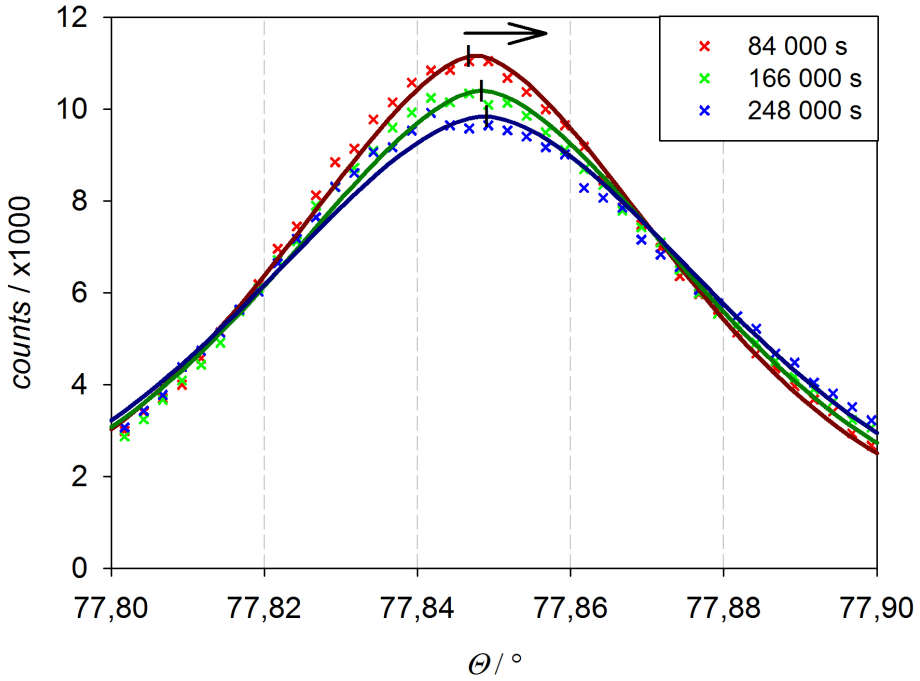

Figure 4.12: Peak shift (311-direction) at various times during isothermal aging at 180 °C.

In Fig. 4.13 the shift of the peak over time for both measurements is plotted. Both curves show a similar total shift, however a significant shift is not seen until 40 000 s of aging. The pronounced shift at the first few measuring points are likely to be due to the shifts of alignment owing to the automatic optimization of z and ω. But also afterwards the measurement point are still fluctuating. This measurement procedure

appears to be at the limit of the diffractometer resolution and is extremely sensitive to any disturbances. As a result, not more information than the overall change in lattice spacing and the average trend of the curves, constant up to 4×10^4 s and then increasing, can be extracted.

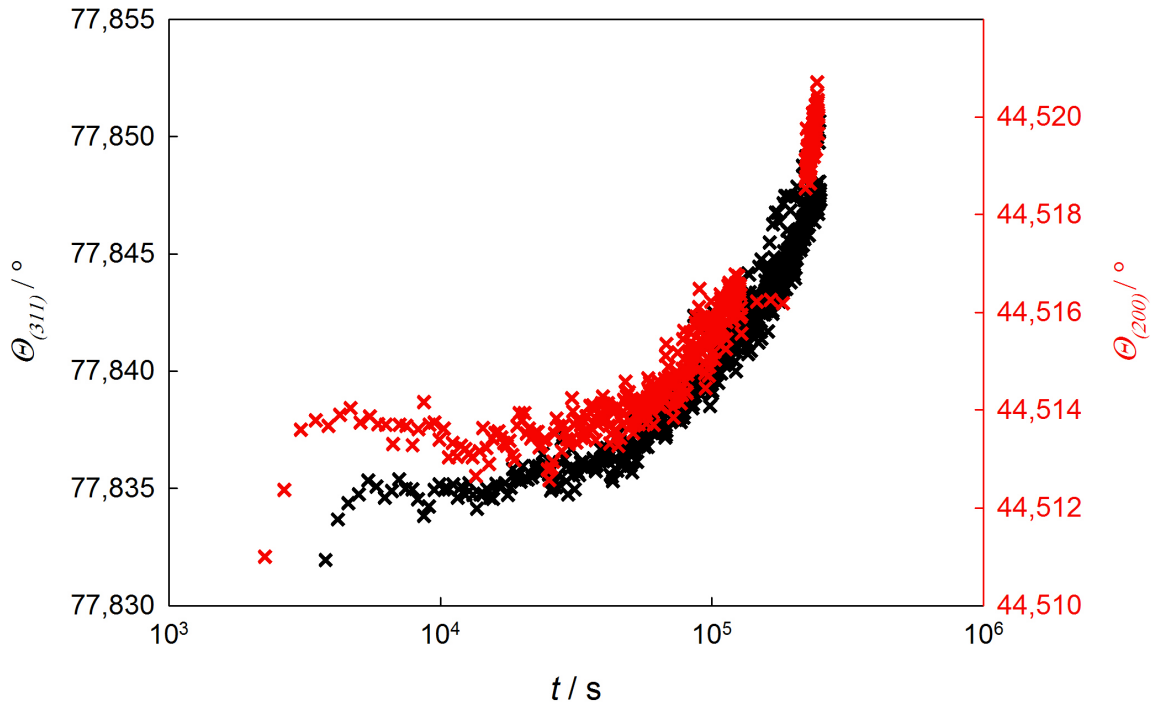

Figure 4.13: Position of (311)- and (200)-peak during isothermal aging at 180 °C.

5 Discussion

5.1 Precipitation Sequence in EN AW-6060

To understand the precipitation and hardening processes in detail, the chronology of precipitates and the atomistic mechanisms behind it must be known exactly. In the case of the Al-Cu system the precipitation sequence is well established in literature. However, for the Al-Mg-Si-system the situation is much more complicated. There are still ongoing discussions about the emerging precipitates, how their atomistic structure looks like, and about the required conditions to form a specific precipitate. Literature research may be aggravated by the fact that the composition and heat treatment condition seems to highly influence the resulting atomic structure and therefore data often get intermixed. Yet, detailed knowledge about the microstructural evolution during aging for the used alloy is essential for discussion of dilatometric or other measurements.

Review articles dealing with the precipitation mechanism in the 6xxx- series of aluminium do already exist (e.g. Ravi and Wolverton[5]). The attempt had always been to consider all possible alloy compositions and heat treatment conditions and to summarize those information into one general precipitation sequence. As a consequence these reviews remain very complex and spotting relevant information for one specific alloy is rather complicated. Before the exact precipitation mechanism can be discussed, a few conventions regarding the nomenclature of heat treatments, alloy composition, and denotation of metastable phases have to be clarified.

In research and also in industry depending on the aging temperature the isothermal heat treatment is labeled differently. Aging at room temperature (RT) is named natural aging (NA), pre-aging (PA) describes aging between 70 °C and 100 °C, and aging at higher temperature, typically around 180 °C, is called artificial aging (AA). If the heat treatment is a combination of those procedures mentioned, it is called a two-step aging. Especially in industry a combination of NA and AA is very common, due to the storage time between forging and paint-baking.

As outlined in Sec. 4 the Mg/Si ratio is 1.6 and the total concentration of the alloying elements Mg and Si is 1.05 at %. It is generally agreed, that an alloy with Mg/Si = 2 is named balanced, as this is the stoichiometric composition of the equilibrium phase Mg_2Si. Accordingly, Mg/Si < 2 is named excess-Si and Mg/Si > 2 excess-Mg. In practice, however, for excess-Si alloys the composition is rather Mg/Si < 1. Therefore, the present alloy is best compared to a balanced alloy. It is also called a low-alloyed aluminium as the total amount is approximately 1. Higher than that would be called high-alloyed.

Often the first two stages are called Guinier-Preston zones (GP-I and GP-II) based on the precipitation sequence of Al-Cu. Depending on the source, the designation varies, sometimes GP-I and GP-II are stages before β'' [17], elsewhere GP-II equals β'' [18]. When it was adopted for Al-Mg-Si systems, the general belief was that the early phases occurring are quite similar to that of Al-Cu. Ongoing research, however, revealed that this assumption is not accurate and attempts for adjusting are very likely the reason for the inconsistency in designation. Therefore, in this work the terms GP-I and GP-II will be left out completely, instead the early stages will be named (Co-)Clusters and pre-β'' . Although the designation was taken from Marioara et al. [19] please note, that the definition given here slightly differs. Here, we stick to a more general description and the initial-β'' (early precursor to pre-β'') is left out.

An overview of the complete precipitation sequence, which can be used for all Al-Mg-Si alloys is already given in Sec. 2.3.1. In the following section an detailed review of the precipitation sequence relevant for the investigated alloy composition in this work will be presented.

Cluster:

Clustering is the first step in the precipitation mechanism. It occurs during or shortly after quenching and can be described as the agglomeration of solute atoms from a super-saturated solid solution (SSSS). Investigation of the cluster formation is complicated due to their small size and hence the small number of incorporated atoms as well as the high coherency with the matrix. For balanced, low alloyed aluminium, the density of precipitates is smaller than that for Si-excess alloys [20] and thus especially for those are even more complicated to investigate experimentally [12].

Apart from simulations, high-angular annular dark field scanning tunneling electron microscopy (HAADF-STEM [21]), atom probe tomography (APT [22]) and positron annihilation lifetime spectroscopy (PALS [23]) may be the most promising techniques for determination of kinetics and atomic structures.

In solid solution, magnesium and silicon occupy substitutional atomic positions, whereby magnesium is expanding the surrounding aluminium matrix and silicon is contracting it. These opposing properties lead to a high driving force to form agglomerates with alternating solute atoms to compensate this size effect [24]. There are reports that even directly after water quenching small clusters are already formed [22,23]. With slower quenching rates, cluster formation becomes larger. Regarding their composition, the total amount of solute and the ratio Mg/Si has a strong influence. Van Huis et al. used the density functional theory (DFT) to calculate the most favourable cluster composition depending on the solute concentration and concluded that great differences can be seen between Mg/Si > 1 and < 1. Short timescales and/or low temperatures (as during NA) enables only local rearrangements because of the limited diffusion length available [25]. Especially for low alloyed materials, longer diffusion length may be needed to form more favourable stoichiometric defined phases. This, once again underlines the fact that clustering is very sensitive to the alloy composition.

Although the detailed clustering kinetics are described differently by various authors, most agree on a multistage clustering process (pronounced at low temperatures, e.g. RT). Examination of these mechanism have mainly been done during NA as kinetics are slower and therefore easier to follow. The most important findings on clustering of low-alloyed balanced aluminium alloy are presented in the subsequent list. For the sake of clarity, please see Tab. 5.1 for the exact heat treatments performed:

- van Huis et al. [24]: Calculations predict that $(MgSi)_2Al_{10}$ and $(MgAl)_1Al_{10}$ are the most favourable clusters for Mg:Si>1 and the morphology is more likely to be platelets than needles.

- Torsæter et al. [25]: The composition of clusters formed during NA is similar to that of the alloy composition, whereby only co-clusters have been detected. In an excess Mg alloy, clusters with Mg/Si ratio of 1 and simultaneously 3 have been determined.

- Murayama et al. [22,26]: Directly after quenching mainly single solute Mg-cluster have been found, which afterwards enrich in Si during prolonged NA. When the ratio becomes approx. 1, Mg-enrichment starts and the clusters tend to reach the ratio of the following phases (β'' and β').

- Matsuda et al. [17]: During aging at 70 °C, fine plates with a Mg/Si ratio of 1 were found. They form alternating columns of Mg and Si.

- Fallah et al.[27,28]: Aging at 180 °C yield three consecutive types of clusters which all coexist at 5 min aging time (as-quenched was not investigated) but then evolve into each other. The initial one is Si-rich but the Mg content rises fast and the last stage is minor Mg-rich. This Mg-enrichment is particular fast in Mg-rich alloys. NA cluster behave similar but rather strive for a Mg/Si ratio of 1.

All publications mentioned above have in common, that more than one different type of cluster is formed during NA and that their composition depends on the composition. However, the composition of the very first small cluster which are nucleating during quenching or directly afterward is still under discussion. One possible explanation for that is given by Edwards et al.[4], who compared the Al-Mg-Si with Al-Mg alloys. In the latter one, it is known that clustering already occur at −30 °C in DSC measurements but already dissolve above 70 °C[20]. Thus the driving force for clustering of Mg atoms in an aluminium matrix is very high but these agglomerates are also very unstable at elevated temperatures. Together with the known difficulties in studying the directly quenched state with any experimental method, deviations in experimental observations seem explicable.

In contrast to the balanced alloys, Si-excess alloys show a different behaviour where it is rather clear that single-solute Si-cluster form first. It is generally agreed, that after quenching single-solute clusters are formed, which then transform or dissolve and become co-clusters.[4,29] The explanation for the transformation kinetics are also deviating for excess-Si alloys .

During natural aging, clusters are stable and only grow over time, whereby the size and hence the hardness increase logarithmically[23,30,31]. But if aging temperatures are higher, clusters aggregate and become more complex in structure with aging time and eventually transform into defined atomic structures.[17]

pre-β'' -phase(s):

Many different precursors to the β''-phase have been reported, which also coexist with each other. It is unclear if a line can be drawn between clusters and pre-β'' as transitions seems to be continuous. One possibility is to denote all agglomerates that have a more or less random atomic ordering as clusters and all precipitates with a distinct periodic crystal structure as pre-β'' .

Regarding the composition and structure of those pre-β'' phases, a wide range of phases have been determined[32] and observations seems to be very hard too. For instance, Edwards et al.[4] concluded that small precipitates form following the co-clusters but

their structure was impossible to resolve. Murayama et al.[22] observed phases with a Mg/Si ratio of 2 after 30 min of aging at 175 °C in a balanced alloy. Van Huis et al.[24] did find Mg_2SiAl_3 and $Mg_3Si_2Al_5$ to be the most favourable precipitates prior to the β'' phase in Mg-rich alloys. For the first one, also the atomic structure and coordinates were given (see Fig. 5.1a).

In Si-excess alloys these precursor phases seem to be more pronounced as indicated by a small peak or plateau in the hardness curve. The structure was determined to be $(Al, Mg)_5Si_6$ which is already quite similar to that of β'' [19,20].

During transformation into β'' only minor structural changes occur when simulations are considered[24,33] but experimental data also reveal dissolution[20].

β'' -phase:

The β'' phase is characterized by being the first non-fcc phase and the particle size is now significantly higher[20]. This makes it fare more easy to determine the crystal structure and composition. Furthermore, for almost all Al-Mg-Si alloys it is well known that β'' is predominant in the peak hardness conditions, which makes it easier to directly compare different publications.

The first to investigate the structure was Murayama et al.[34] who determined the lattice parameters and the Mg:Si ratio (1.74 ± 0.07) of a balanced-alloy. The presence of aluminium, however, stayed unknown. An excess-Si alloy was also examined, whereby it was concluded that the Mg/Si ratio of all metastable phases depend on the alloy composition. Matsuda et al.[32] conducted TEM and X-ray measurements on a Si-excess alloy and presented the composition for the β'' phase as well as the space group and lattice parameters ($Mg_1Al_3Si_6$).

Almost simultaneously, Andersen et al.[35] did also TEM studies of an alloy quite similar to that investigated in the present work. They had to make several assumption to be able to clarify the composition, among them that aluminium is not present in the β'' phase. With these constraints, Mg_5Si_6 was presented as the stoichiometric composition of the precipitate although it was noted that a Mg/Si ratio smaller than 1 was surprising.

Later, Hasting et al.[36] revised those findings and added atom probe tomography (APT) measurements and DFT calculations (now using a Si-excess alloy). It was found, that replacing some Si atoms with Al atoms provide a likelier atomic structure and therefore corrected the chemical composition to be $Mg_5Al_2Si_4$.

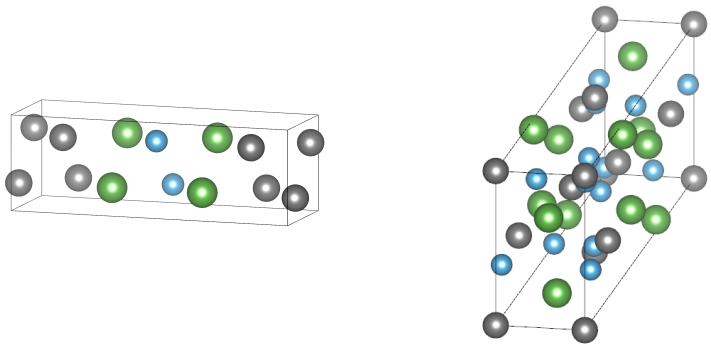

(a) pre-β'' [24] **(b)** β'' [21]

Figure 5.1: Atomic structures [1] of one possible pre-β'' (Mg_2SiAl_3) and the β''-phase ($Mg_4Al_3Si_4$) grey: Al, green: Mg, blue: Si.

Finally, Ninive et al.[21] and Ehlers et al.[38] conducted HAADF-STEM measurements and also DFT calculations but now including the precipitate formation energy and the strain fields. Microscopy indicated that the Mg-positions also contain aluminium and raise $Mg_4Al_3Si_4$ (see Fig. 5.1b) as the likest composition. However, according to DFT calculations, $Mg_5Al_2Si_4$ still has the lowest precipitate energy and should therefore be the most stable one. From detailed considerations of the interface strain field it was concluded that the interface structure is more stable when containing additional Al. As the atomic radius of Al is smaller than that of Mg, replacement of Mg is likely. Combined with the circumstance, that precipitate growth is inside-out directed, $Mg_4Al_3Si_4$ is also stable from a theoretical point of view.

When transformation of the β''- into the β'-phase is considered, both dissolution and transformation seem to be possible. Tsao et al.[39] reported separate nucleation and growth mechanism for both the β''- and β'-phase. Therefore, β'' dissolves and simultaneously β' nucleates and grows.

This transition also marks the shift from coherent to semi-coherent precipitates. In terms of the hardness response, precipitation of the following phases results in a decay.

β'-, U1-, U2-, B'- phase:

Among all stages in the precipitation sequence of Al-Mg-Si alloys, the overaging regime has been studied most extensively. The early stages are more important for the optimization of the hardening process but the later ones are much easier to analyze.

1 Data were taken from the articles cited next to the structure and were visualized with VESTA3 [37]. All structures were plotted in the same orientation.

The particles are relatively large, have a well defined structure and are stable in a wide temperature range. That is the reason why research focused on this regime for a long period of time.

In the very first attempts to clarify the microstructure of the metastable phases, it was believed that only one phase appears. But soon, other coexisting phases have been identified and now 4 different phases (β', U1, U2 and B') are known to exist depending on the alloy composition and previous heat treatment.

Information about which phases occur at which condition (β', U1,U2 or B') and if they are coexisting is very important. The following data could be obtained for a balanced Al-Mg-Si alloy:

- Andersen et al.[40]: U2 coexist with β'' and β' but many precipitates are of β' and U2.
- Marioara et al.[20]: No U1 was detected and the amount of U2 is very low. At peak aged both β'' and β' exist.
- Marioara et al.[41]: β' is predominant, no B', U1 or U2 was detected.
- Matsuda et al.[42]: Type A, B and C do coexist after 60 000 s at 250 °C in an excess-Si alloy whereas in an balanced alloy, β' seem to be the predominant precipitate.
- Matsuda et al.[43]: β'' is less pronounced in a balanced alloy than in a Si-excess one, Type A, B and C are not present at all but the amount of β' is high.

Jacobs et al.[44] managed in 1972 to identify the β'-phase as rod-shaped and quantified the lattice parameters.

The U1- and U2- phases have both been investigated by two different research groups independently. As the resulting chemical compositions are deviating, different designations were established. The U1-phase (U2-phase), denoted so by Andersen et al.[40,45], was named Type A (Type B) precipitate by Matsuda et al.[42,46,47]. Both groups used a Si-excess alloy but a closer look on the proposed chemical composition reveal that for both phases Matsuda et al. may have underestimated the Mg- content. That TEM-preparation is very critical regarding the oxidation of Mg has already been reported[41]. Andersen et al.[40,45] supplemented their HRTEM measurements by conducting DFT calculations and X-ray spectroscopy. Because of that, here the composition proposed by Andersen seems more reliable and will be used for further analysis.

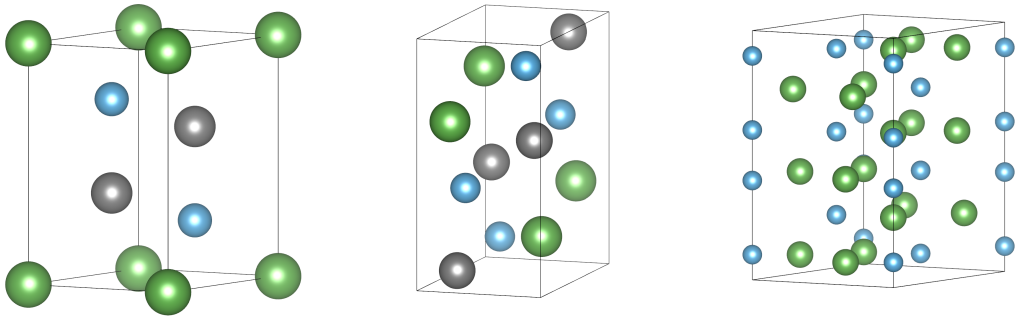

(a) U1 [45] **(b)** U2 [40] **(c)** Mg_9Si_5 β' [36]

Figure 5.2: Atomic structures[1] of U1 ($MgAl_2Si_2$), U2 (MgAlSi) and β'-phase (Mg_9Si_5), grey: Al, green: Mg, blue: Si.

In contrary to the U1- and U2-phases, not much is known about the B'-phase. As this phase only occur in small concentration, it was not possible to determine the exact chemical composition or the atomic structure up to now [42].

The structure of the β'-phase is already very similar to the equilibrium phase β. The Mg/Si ratio has only to rise from 1.8 to 2 but instead of transformation from β' to β, decomposing and separate nucleation have been reported. Also coexisting of these two phases have been reported [42].

β-phase:

The equilibrium phase was historically the first which was studied in detail. Geisler et al. (1947) investigated a balanced alloy by electron microscopy after aging at high tempertures and identified the β- phase to be Mg_2Si, having a fcc, Ca_2F-structure [48]. It have been reported that it is not forming below approx. 300 °C [41,43].

Both Zandbergen et al. [6] and Murayama et al. [22] concluded that the precipitation sequence of Al-Mg-Si is rather a continuous process with continuous evolving precipitates than consisting of distinct states.

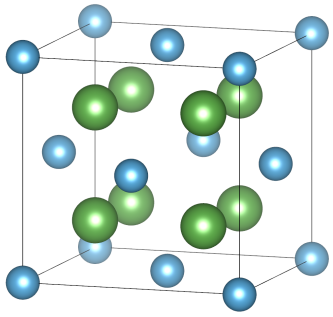

Figure 5.3: Atomic structure[1] of Mg_2Si (β-phase) [48], grey: Al, green: Mg, blue: Si.

Tab. 5.1 summarizes the most important publications on the various types of clusters and precipitates. It should be mentioned, once again, that the summary is restricted to aluminium alloys with approx. 0.6 at % Mg and 0.4 at % Si; other concentrations may show different behaviour [5,20,39,41,43,49], especially regarding the first stages of precipitation. Data taken from articles, in which Si-excess alloys are discussed, are marked in the table. They were included because at longer aging times,

the prolonged time for diffusion may reduce to dependence of the precipitate structure on the exact composition of the alloy.

Natural aging prior to artificial aging:

In industry, a storage time between annealing and aging (paint-baking) is nearly unavoidable. Also in research natural aging has often been performed prior to artificial aging which was either chosen to simulate industrial heat treatments or was also unavoidable because of technical reasons. In the present work, 4 min of natural aging had to be included.

The distinct features of these two-step heat treatments are mainly due to the cluster formation during natural aging, which are stable (or unstable) at higher temperatures during artificial aging.

There are several publications on the evolving processes following a two-step heat treatment, comparing similar alloys and heat treatments the findings are fitting very well.

Murayama et al.[22], Grau et al.[31], Serizawa et al.[50] and Fallah et al.[27] reported that cluster formed during natural aging dissolve after heating to temperatures higher than 100 °C. Clusters originating from preaging (approx. 70 °C) are evolving and transforming into pre-β'' and β'' during artificial aging. Murayama et al.[22] explained this phenomena in terms of the critical radius for nucleation. The radius of NA-cluster is too low to reach the critical radius needed for nucleation at the elevated temperatures during artificial aging.

Type	**Chemical composition**	**Occurrence**	**Comments**	**Alloy specification**	**Reference**
Cluster	Mg-cluster, which aggregate to co-cluster (Mg/Si=1)	as-quenched	extremely fine		Murayama et al.[22], 1998
	separate Mg and Si cluster, later Co-Cluster	NA (70 days), aged at 175 °C			Murayama and Hono[26], 1999
	Mg/Si varying from 1 to 2	NA (7 days), aged at 170°C	cluster-type after NA and PA differs		Serizawa et al.[50], 2008
	$(MgAl)Al_{10}$ and $(MgSi)_2Al_{10}$		1-3 nm (spherical)		van Huis et al.[24], 2007
	Mg/Si=1 and other Mg-rich	NA (7 days), preaging for 16 h			Torsæter et al.[25], 2007
		5 to 20 min aged at 180 °C	three types evolving into each other		Fallah et al.[27], 2016; Fallah et al.[28],2015
pre-β''	Mg_2SiAl_3, $Mg_3Si_2Al_5$		platelets; atomic structure of $Mg_3Si_2Al_5$ given		van Huis et al.[51], 2006
	$(Al^+Mg)_5Si_6$	11 hours at 150 °C	structure is similar to β''	excess Si	Marioara et al.[19], 2001
	Mg:Si=2:1	30 min at 175 °C	needle shaped		Murayama et al.[22], 1998

Type	Chemical composition	Occurrence	Comments	Alloy specification	Reference
	Mg:Si=1	aging at 70 °C	alternating columns of Si and Mg, fine plates		Matsuda et al.[17], 1998
β''	Mg/Si=1.74±0.01	at 175 °C for 32.4 ks	presence of Al unclear		Murayama et al.[34], 1997
	Mg:Si:Al = 1:6:3	at 150 °C for 2400 ks	monoclinic with space group P2/m; full atomic structure resolved	excess Si	Matsuda et al.[32], 1999
	Mg_5Si_6		needles of 4x4x50nm; full atomic structure resolved		Andersen et al.[35], 1998
	$Mg_5Al_2Si_4$	36 h at 175 °C; 45 min at 220 °C	mean cross section of 5.27 ±0.23 nm^2	excess Si	Hasting et al.[36], 2009
	$Mg_4Al_3Si_4$				Ninive et al.[21], 2014
U1	$Mg_1Si_2Al_2$	3 h at 260 °C	needles of several hundred nm long and 15 nm diameter	excess Si	Andersen et al.[45], 2007
	Si:Al:Mg=5:4:1	60 ks at 250 °C	rod-shaped, named as Type A	excess Si	Matsuda et al.[42], 2000; Matsuda et al.[46], 1995
U2	$Mg_4Si_4Al_4$	208 hours at 175 °C	atomic structure resolved	excess Si	Andersen et al.[40],2005

Type	Chemical composition	Occurrence	Comments	Alloy specification	Reference
	Si:Al:Mg=5:4:2	60 ks at 250 °C	orthorhombic, named as Type B	excess Si	Matsuda et al.[42], 2000; Matsuda et al.[47], 1996
B'			ribbons up to 1 μm		Zandbergen et al.[6], 2015
	Si/Mg= 1.22, Al unknown		hexagonal		Matsuda et al.[42], 2000
β'	Mg_9Si_5	NA (4 days), aged at 260°C (3 h)	rods several hundred nm long with 10 nm diameter; exact atomic structure resolved		Vissers et al.[52], 2007
		several hours at 250 °C	rod-shaped		Jacobs[44], 1972
	Mg/Si=1.68	12 ks at 250 °C	hexagonal, rod shaped		Matsuda et al.[53], 1993; Matsuda et al.[42], 2000
	Mg:Si = 1.75±0.03	3.6 ks at 250 °C	hexagonal; two types of precipitate present		Murayama et al.[34], 1997
β	Mg_2Si	plates or cubes up to 10-20 μm			Geisler and Hill[48], 1948

Table 5.1: Overview of presumable precipitation sequence for EN AW-6060

5.1.1 Primary phases

To some extent industrial aluminium alloys always contain secondary alloying elements as well. Mostly, it is either iron or manganese, but chromium, zirconium, vanadium, or titanium are also common. The present AW-6060 alloy contains 0.11 at% iron and 0.006 at% titanium which are forming $Al_{14}Fe_3Si_3$ and $Ti_7Al_5Si_{14}$ in equilibrium conditions (Tab. 4.1 and Fig. 4.1). Iron forms primary precipitates (also known as dispersoids) during solidification because of its low solubility. They do not influence the strength significantly and are stable up to 500°C to 550°C, thus are stable during homogenization. Depending on the cooling rate from the melt different chemical compositions arise which often includes silicon too[54],[13],[55]. This reduces the amount of silicon available for precipitation hardening and simulations are necessary to be able to make an estimation. For the precipitation mechanisms itself, dispersoids may play an important rule. If the cooling rates are too low, they could act as premature heterogeneous nucleation sites for Mg or Si. Manganese or chromium containing particles can also influence the homogenization behaviour as they are not stable in this temperature regime[55–57].

5.1.2 Quantitative estimation of precipitation-induced volume change

Based on the data obtained by diligent literature research, a rough estimation of the volume change during isothermal annealing is possible. This is needed to correlate a length increase or decrease to a specific phase. Milkereit et al.[8] did non-isothermal dilatometric study of Al-alloys and concluded that the overall length change depends on the interplay of precipitate growth and reducing solute content in the matrix. Whether this results in an overall dilatation or reduction depends on the type of alloying elements and precipitate structure that is formed.

For a quantitative estimation, besides the lattice parameters and atomic structures of the precipitates, which have been extracted from the publications listed in Tab.5.1, some additional data is needed:

- Lattice constant of pure aluminium[58]: $a_{Al} = 4.04964\,\text{Å}$
- Coefficient of thermal expansion for pure aluminium[59]: $CTE = 23.6 \cdot 10^{-6}\,\text{K}^{-1}$
- The amount of silicon bound in primary precipitates as $Al_{14}Fe_3Si_3$ and $Ti_7Al_5Si_{14}$ (see Sec.3).

- Change in lattice spacing due to variable amount of alloying elements. Linear correlation was determined by Pearson [60](p.346, Fig.59)

$$\begin{aligned} \text{for magnesium: } \Delta a_{Mg} &= (0.0100202/2.2) \times at\%\text{Mg} \\ \text{for silicon: } \Delta a_{Si} &= (-0.0100202/6.8) \times at\%\text{Si} \end{aligned} \tag{5.1}$$

Furthermore, the following assumptions and simplifications were made:

- Overall number of atoms is constant.
- Contribution of Mg and Si to lattice spacing (Eq. 5.1) in the aluminium matrix add up.
- All silicon atoms who are left unbound to primary precipitates are available to form secondary precipitates. This supposes diffusion lengths are large enough. Furthermore, due to the lack of available data, the solubility of magnesium and silicon at elevated temperatures is not considered.
- Primary precipitates are completely inert.
- Coefficient of thermal expansion is equal for all precipitates and corresponds to that of pure aluminium.
- A perfect single crystal is considered. No effects from vacancies, dislocations, grains or grain boundary are taken into account.
- Volumetric contribution of interfaces and strain field around a precipitate are neglected.
- In equilibrium, the excess Si forms Si-precipitates in diamond structure. For correct estimation of the volume change when reaching equilibrium conditions, the influence of those pure Si-precipitates would have to be included. As no experimental data at that conditions were performed, these precipitates have not been considered.

For each step simply the volumetric changes of the aluminium-matrix and the precipitates are calculated. The thermal expansion for the whole material is isotropic, so the volumetric thermal expansion coefficient (α_V) can be approximated to be three times the linear expansion coefficient, i.e.

$$\frac{\Delta V}{V_0} \approx 3 \times \frac{\Delta L}{L_0}. \tag{5.2}$$

Considering these aspects, four different states can be identified during the precipitation sequence, which are visualized in Fig. 5.4. For clarification the crystal structure has been simplified and the alloy concentrations magnified. For each state, the residual solid solution (all Mg and Si-atoms that cannot be included into precipitates) have also been considered.

(a) Super-saturated solid solution (SSSS) with Mg- and Si-atoms that are expanding or contracting the matrix

(b) Coherent precipitates that enlarges the overall volume with the corresponding SSSS.

(c) Same as b) but the precipitates reduce the volume

(d) Incoherent precipitate, whereby the influence of the interface is unknown.

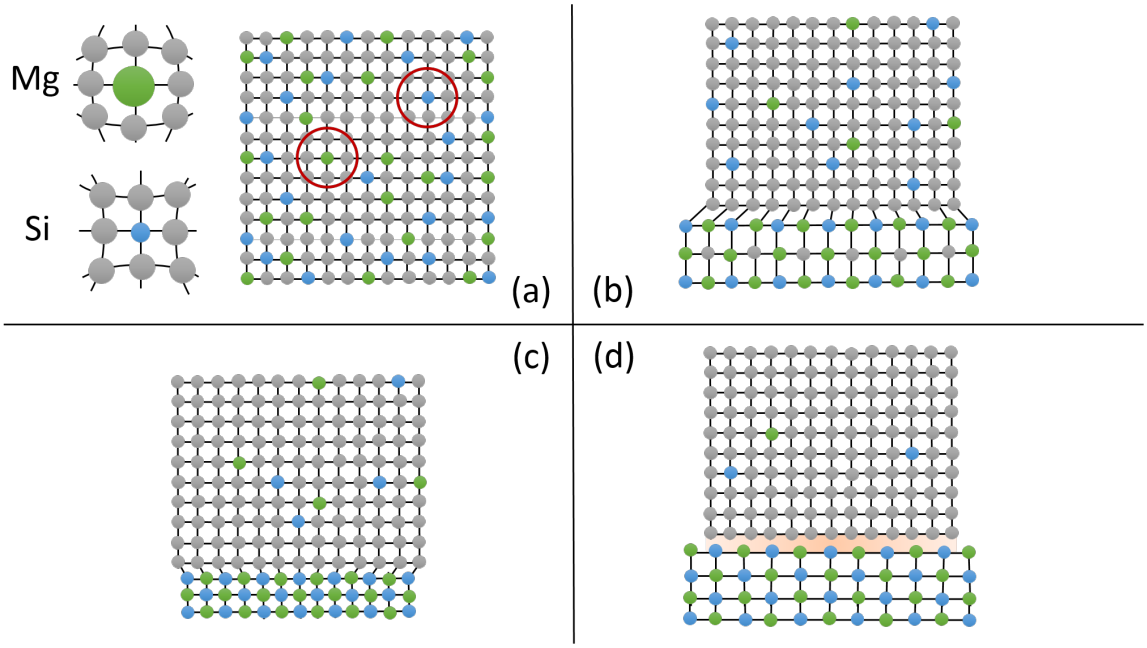

Figure 5.4: Influence of the precipitation of different phases on the overall volume. (a) SSSS, (b) and (c) coherent precipitate and (d) incoherent precipitate

Steps for calculation:

The evaluation of the quantitative volume change due to precipitation was done for a constant number of atoms, consisting of 0.41 at%Si, 0.64 at%Mg and balanced aluminium.

Subsequently, the steps for calculation the volume change are listed.

1. For the precipitate phase, the volume of one unit cell v_{prec}, as well as the number of Mg, Si and Al atoms in one cell was extracted from literature.

2. Then the lattice parameter a_{SSSS} and hence the volume V_{SSSS} of the SSSS was calculated by means of Eq. 5.1

$$\Delta a_{SSSS} = \Delta a_{Mg} + \Delta a_{Si} \tag{5.3}$$

$$a_{SSSS} = a_{Al} + \Delta a_{SSSS} \tag{5.4}$$

$$V_0 = (a_{SSSS})^3 \tag{5.5}$$

3. Next the number of unit cells N_{prec} that are formed during precipitation is calculated. This is done by determining the maximum number of unit cells that can be formed considering the stoichiometric concentration of the precipitate phase. Therefore, for both Mg and Si, the total number of atoms in the material is divided by the number of atoms in one unit cell (which was taken from literature). The lower number is then the number of unit cell that can form. All atoms of Mg and Si that could not be incorporated in the precipitate phase have to be considered in the remaining solid solution (step 5).

4. The volume taken by the precipitate phase is than calculated by

$$V_{prec} = N_{prec} \times v_{prec}. \tag{5.6}$$

5. Before calculating the total volume change, the volume of the aluminium matrix with the residual Si and Mg ($V_{residual}$) has to be determined which is done similar to step 1, but the reduced concentration of Mg and Si are now used for calculation.

$$\Delta a_{residual} = \Delta a_{Mg} + \Delta a_{Si} \tag{5.7}$$

$$a_{residual} = a_{Al} + \Delta a_{residual} \tag{5.8}$$

$$V_{residual} = (a_{residual})^3 \tag{5.9}$$

6. The total volume after precipitation is then determined

$$V_{after} = V_{prec} + V_{residual}. \tag{5.10}$$

7. To finally determine $\Delta L/L_0$, first $\Delta V/V_0$ must be calculated by

$$\frac{\Delta V}{V_0} = \frac{V_{after} - V_0}{V_0} \tag{5.11}$$

and then $\Delta L/L_0$ is determined by Eq. 5.2

$$\frac{\Delta V}{V_0} \approx 3 \cdot \frac{\Delta L}{L_0}. \tag{5.12}$$

Those values can then be directly compared to dilatometric measurements.

In Tab. 5.2 the precipitates that have been evaluated are listed. The cited publications correspond to the source of the atomic structure and lattice parameters. Three different chemical compositions for the β''-phase have been considered in the calculation. They all have the same structure, only the atomic positions are occupied by different elements. However, Ninive et al.[21] have already identified $Mg_4Al_3Si_4$ to be the most likely chemical composition.

Column 5 ($\Delta L/L_0$) can directly be compared to the measured length change seen in Fig. 4.5, which immediately reveal that the calculated length change fits the measured one according to its order of magnitude. For detailed comparison the calculated values have been included in the dilatometric curve and can be seen in Fig. 5.5, (C), which is presented below.

In step 5 the lattice constant of the aluminium matrix with the residual Mg and Si was calculated. $\Delta a_{residual}$ represents the difference between this residual solid solution

and pure aluminium. However, for comparison with the experimental data the change in lattice constant from SSSS to the residual solid solution (Δa_P) is needed.

$$\Delta a_P = a_{residual} - a_{SSSS} = \Delta a_{residual} - \Delta a_{SSSS} \tag{5.13}$$

$$\Delta a_{SSSS} = 23.1 \times 10^{-4}\text{Å} \tag{5.14}$$

In column 6 (Δa_P) the change in lattice constant of the aluminium matrix compared to the SSSS is listed for each precipitate. The results can be directly compared to Fig. 5.5 (B), which is discussed below.

Table 5.2: Estimated volume change due to precipitation.

Phase	composition	system	space group	$\Delta L/L_0$ / $\times 10^{-5}$	Δa_P / $*10^{-4}$Å
(β'') [36]	$Mg_5Si_4Al_2$	monoclinic	C2/m	-7,5	-17.3
(β'') [35]	Mg_5Si_6	monoclinic	C2/m	-0.2	-9.5
β'' [21]	$Mg_4Al_3Si_4$	monoclinic	C2/m	3,9	-12.4
U1 [45]	$Mg_1Si_2Al_2$	tetragonal	P-3m1	43.6	-3.3
U2 [40]	MgSiAl	orthorombic	Pnma	5,1	-12.6
β' [52]	Mg_9Si_5	hexagonal	P63/m	-6,9	-23.9
β [48]	Mg_2Si	fcc	Fm-3m	28.5	-24.4

5.2 Precipitation Kinetics during Aging

Combining the data obtained from dilatometry, XRD and hardness test as well as literature research and the volume change approximation, it is now possible to clarify the kinetics underlying the age hardening of AW-6060.

To shortly summarize the information given in Sec. 5.1 and to ease the discussion of the measured dilatometric curves, the following list presents the precipitation sequence which is likely to occur in AW-6060 during heat treatment in the dilatometer after quenching and NA for 4 min (see Fig. 4.2).

1. During NA, formation of seperate Mg-/Si-clusters occurs, which are then partially dissolving or transforming into co-cluster (balanced and Mg-rich).
2. When heating to AA, co-clusters start to evolve into pre-β'' and/or β''.
3. Some β'' precipitates begin to transform into β' and U2 while other are still growing. The aging temperature thereby determines the transformation rate and the relative concentrations of the coexisting phases.
4. At temperatures higher than approx. 300 °C, the β- phase is formed after prolonged aging.

In Fig. 5.5 the relevant results for analysis are presented together. All three plots have one curve in common, the length response upon artificial aging at 180 °C (blue). Additionally, the first one (A) also contains the length change at 210 °C (red) and the last one (C) 210 °C and 240 °C (grey). In (A) the hardness data, as already presented in Fig. 4.10a, are plotted. (B) includes the results obtained from XRD-measurements, which have been calculated from the detected peak shift in Fig. 4.12 by using Eq. 3.1 and Eq.3.2. No data could be received before 2000 s of aging as this time was needed for aligning the sample in the diffractometer.

In the last plot (C), the dashed lines correspond to the calculated length change according to Tab. 5.2. Only those phases which are likely to occur in a balanced, low-alloyed Al-Mg-Si alloy have been incorporated. These are β'' ($Mg_4Al_3Si_4$), U2 and β'. As a base line, the SSSS was also included. The equilibrium phase β is not occurring at the temperatures investigated, therefore has been left out.

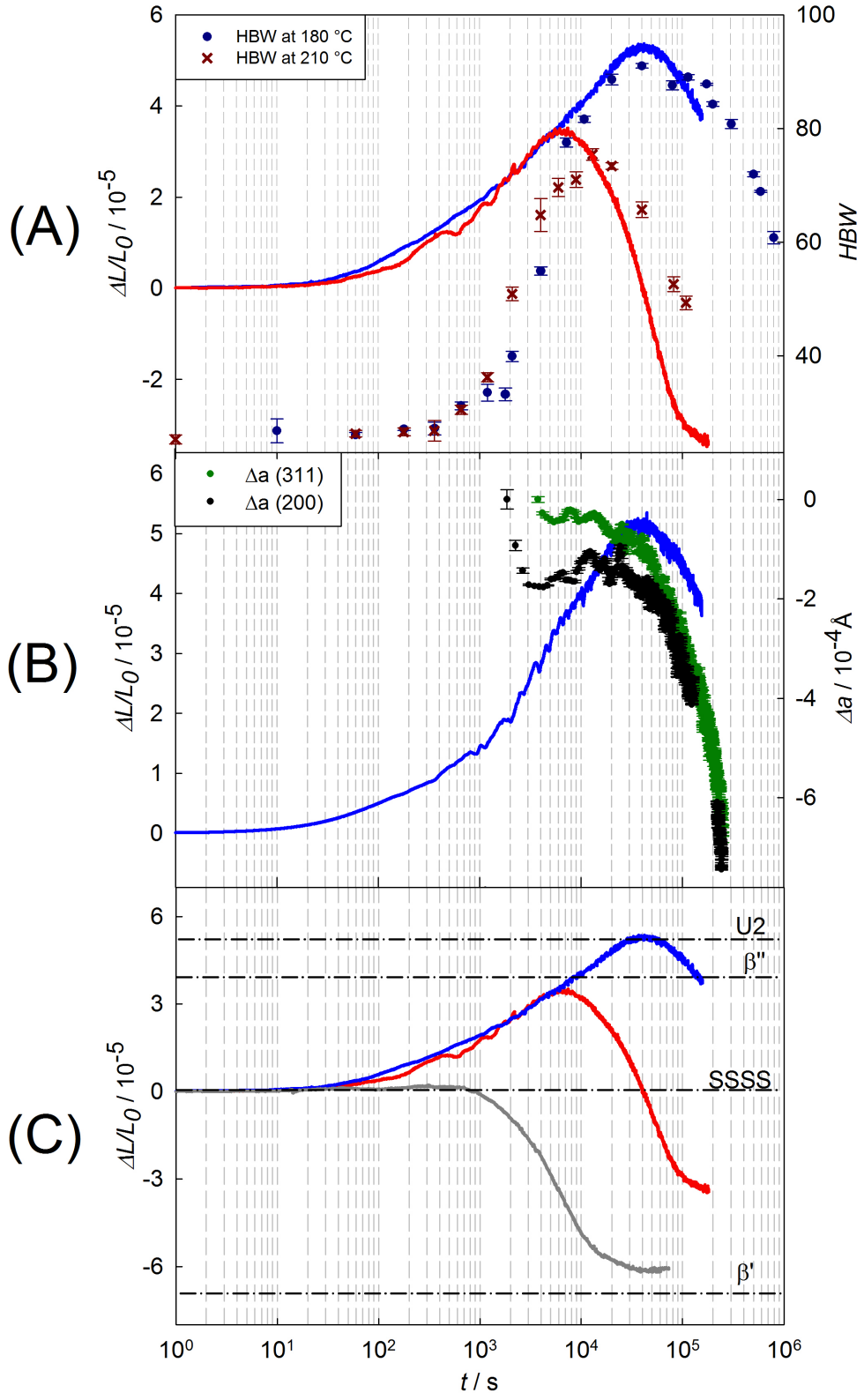

Figure 5.5: Comparison of all relevant data.
Dilatometric curves are seen in each plot at 180 °C (blue), in (C) also aging at 210 °C (red) and 230 °C (grey) are added. Additionally, hardness tests (A), change in lattice constant of the matrix (B) and volume approximation (C) are shown.

Two main obstacles influenced nearly all measurements done in the dilatometer. Both took place during the dissolution process but had also an impact on the length response during aging. Firstly, the formation of an oxide surface layer which reduces the thermal conductivity of the outer layer of the sample and which complicates the process of defining an onset point (see Sec. 4.2.1). Secondly, when performing the measurements in argon atmosphere, the evaporation of magnesium influences the measurements. Although the evaporation does not take place during aging but only at elevated annealing temperatures, reducing the amount of one alloying component will automatically result in a change in the Mg/Si ratio. As explained above, the consequences of this process may be very complex and further analysis is impossible. For instance, M38 (Fig. 4.4) was one of the measurements done under argon atmosphere. The dilatometric curve clearly shows deviation from the other aging experiments at 210 °C, which are plotted in Fig. 4.4.

To ease the comprehensibility, at first only one aging temperature, namely 180 °C will be discussed. Influence of the temperature will be considered in the next paragraph.

5.2.1 Isothermal aging at 180 °C

The length response upon isothermal aging (Fig. 5.5) can be divided into three different segments. The clustering regime up to approx. 100 s, the length increase up to 40 000 s, and the following decrease for longer times.

In the first segment, the length response as well as the hardness do not show a significant change. The dissolution and transformation of co-cluster as well as the formation of nano-scale precipitates of pre-β'' are simultaneously proceeding and their contribution to the length change are overlapping. They are either compensating each other or are too small to be detected at all. The hardness curve to not respond to these microstructural changes because the nuclei as well as very fine precipitates are too small to hinder movement of dislocations (see Sec. 2.2).

For the dilatometric curves, two effects have to be taken into account in the first regime. It is the only one to be highly influenced by the choice of onset point (see Sec. 4.2.1) and secondly, the logarithmic representation is slightly altering the visual information provided. Especially the last one could magnify any influence of small fluctuations in the first few hundred seconds of aging which should be taken into account in order to avoid misinterpretation. Regarding the choice of onset, it has to be considered that the time between reaching the target temperature for the first time and complete equilibration (which equals the onset point) was about 200 s. Any information of the

length change during this period is lost. Yet, there is high potential to enable an earlier onset point by optimizing the PID parameter and the specimen preparation (to avoid oxidation during annealing). This, however, exceeds the scope of this work.

In the second segment the length start to rise steadily and reaches its maximum after 40 000 s. The hardness, however, stays constant for another 400 s, than rises rapidly and also reaches its maximum at 40 000 s of aging. The correlation of the hardness and the length change peak reveal that β'' is predominant at that condition [61]. The flattening of the dilatometric curve is probably due to the already starting nucleation and growth of the β'-phase. There are several publications that observe different type of precipitates at peak aged condition.

These findings coincide with the length calculations shown in Fig. 5.5 (C). Formation of the β''-phase results in an length increase $\Delta L/L_0$ of approx. 4×10^{-5} and formation of β' is reducing the length ($\Delta L/L_0 = -7 \times 10^{-5}$) according to Tab. 5.2. In a balanced Al-Mg-Si alloy, U2 was observed to be coexisting with the β''- and/or β'-phase. Complete transformation into U2 would result in an expansion of 5×10^{-5} which means partially transformation into U2 will at least raise the length increase.

The lattice spacing of the aluminium matrix (Fig. 5.5(B)) is, on average, not changing significantly in this time regime between 2000 and 40 000 s. This enables two different interpretations that are feasible. The first one would be that the some β''-precipitates start to transform into β' but barely no Mg or Si is withdrawing from the matrix or dissolved back into it. Because of the growing contribution of the length reduction from the β' precipitates, the dilatometric curve is flattening. The other possibility would be that the dissolution of one part of β'' precipitates and the formation of β' are compensating each other in terms of the average lattice spacing of aluminium. As the hardness is still increasing, other β'' precipitates still have to grow in size.

After the maximum in length is reached, the last segment starts, at aging times longer than 40 000 s. The length as well as the hardness decreases, this range is now also called overaging regime. Also the lattice spacing of aluminium changes significantly, the total change is approx. -8×10^{-4}Å.

Depending on the amount of Mg and Si atoms needed for the atomic structure of the precipitate, more or less Mg (and Si) remains in the matrix. The β''-phase has an Mg/Si ratio of 1, whereas the β'-phase has a ratio of 1.8, which means that more Mg is precipitating from the matrix into those precipitates during transition from β'' to β'. In solid solution Mg on Al lattice sites is expanding the lattice constant and hence

precipitation of Mg from the matrix is reducing the lattice constant. A reduction of the lattice constant is indeed observed experimentally (Fig. 5.5 (B)).

The measured change of approx. -8×10^{-4}Å can be directly compared to the values obtained in Tab. 5.2 (last column). There the change in lattice constant is referenced to the SSSS, meaning the starting point for aging. To compare the change between precipitation of β'' and β', the values for these two phases must be subtracted from each other, which results in a change in lattice spacing of -11.5×10^{-4}Å. This value is slightly higher than that obtained experimentally but for calculations a variety of assumptions have been made. One among them, is that every Mg and Si atom is actually available for precipitation. In fact however, finite diffusion lengths and a remaining solubility of Mg and Si in Al may hinder that.

5.2.2 Temperature dependence

The precipitation process, as explained above for aging at 180 °C, can be translated quite well to other temperatures. When the temperature increases, phases from later stages in the precipitation sequence nucleate earlier. On the other hand, phases that are forming early at 180 °C may be skipped completely at higher temperatures. Fig. 5.5(C) and Fig. 4.5 show, that the length increase due to β'' is nearly vanishing at temperatures higher than 240 °C. At 240 °C the length remains constant until 800 s which can be interpreted that a small amount of β'' is nucleating/growing but nucleation of β' starts also very early. The following reduction is caused by the formation of β' and is shifted to earlier times when temperature rises. For aging at 210 °C also hardness tests were conducted. They show the expected trend but the curve is shifted slightly to longer times compared to the length response. The peak hardness is shifted by about 4 000 s compared to the length peak. This seems odd at first sight, but considering the superposition of growing β'' (which are responsible for the hardness increase) and the nucleation of the β'-phase (which are reducing the length significantly), this behaviour appears to be reasonable. The dilatometric measurements are much more sensitive to the types of the precipitates, whereas hardness tests only reflect the density and size of coherent precipitates.

At 260 °C the decrease of $\Delta L/L_0$, which indicates the formation of β', starts immediately after reaching isothermal condition. This means that precipitatation prior to the β'-phase is skipped.

At the end of the precipitation sequence, the equilibrium phase β occurs. However, experiments have already shown that β does not form at 180 °C aging temperature[41].

This is confirmed by the observation that the dilatometric curves are stable after reaching the plateau. Calculations reveal that the β formation would result in a length increase which is 4 times larger than the increase caused by formation of the β'' phase (Tab. 5.2) .

Comparing all dilatometric curves in Fig. 4.5 and the calculated length change in Tab. 5.2 as well as Fig. 5.5, one may notice that depending on the temperature, the measured values for length change exceed the calculated ones. In detail, aging at 170 °C exceeds the calculated values for β'' and U2 and aging at 260 °C exceeds the value for β' (Fig. 4.5). The conducted approximation for the volume change is only a rough estimation. Some important influencing factors had to be left out. In particular, strain fields and interfaces have been already reported to have a high impact on the precipitation mechanism, hence probably will also influence the volume greatly. Both have not been considered in these calculations.

5.2.3 Natural aging

Natural aging is defined as aging at approx. 20 °C and is often discussed completely separately to other aging mechanisms. However, detailed literature research and comparing them with the data obtained in this work (Fig. 4.7), reveal that natural aging can be explained using similar approaches.

Neither β'' nor any other phases than co-clusters can form at that low temperatures. But co-clusters are reported to grow in size during NA and thereby become detectable for the dilatometer. The trend of the curve corresponds well with the hardness curve measured. Also in literature[62,63] a nearly logarithmic increase in length was reported. Elsewhere, clustering was reported to evolve for approx. two weeks and remains nearly constant afterwards. This also could be confirmed by dilatometry, as the length increase flattens at the end of measuring time (Fig. 4.7).

However, it should be mentioned, that NA was conducted at slightly higher temperatures, at 30 °C and 40 °C. Hence, a nucleation and growth of pre-β'' might be possible but further analysis would be needed to confirm or disprove it.

5.2.4 Activation energy

By using the Arrhenius equation (see 2.1, Eq. 2.3)an apparent activation energy can be deduced from the peak positions in Fig. 4.5. The resulting Arrhenius plot can be seen in Fig. 5.6, the activation energy was determined to be:

$$E_{A,p} = (109 \pm 7)\text{kJ/mol}. \tag{5.15}$$

The position of the maximum length change is influenced by two processes going on in the material. First the formation and growth of the β'' phase causes the length to increase, later the transformation into β' takes place, which causes the length change to flatten first and then to decrease. Based on that assumption, it can be concluded, that the apparent activation energy E_A is related to the formation of β'-precipitates.

Daoudi et al.[64] determined the apparent activation energy for the β''-phase by using non-isothermal dilatometry. They concluded, that the activation energy rises with increasing fraction of the transformed β''-phase, from 77 kJ/mol up to 110 kJ/mol. When comparing the absolute values, it is important to know, that the alloy composition significantly varies from that examined in the present work, which means this values may differ.

However, regarding the dependence of the activation energy on the transformed fraction, some similarities may be found. Therefore, in Fig. 4.5 the inflection points that occur during the decrease in length following the maximum length increase, may be used for further analysis. Although no information of the exact amount of transformed phase is available, according to the interpretation of the dilatometric response presented in Sec. 5.2.1 and 5.2.2, those inflection points can be regarded as a state where more β' is present then at the peak positions. By using these positions, the apparent activation energy is determined to

$$E_{A,i} = (160 \pm 60)\ \text{kJ/mol}. \tag{5.16}$$

Comparing $E_{A,i}$ and $E_{A,p}$ as well as considering the findings by Daoudi et al.[64], it may be concluded, that the activation energy increases with the transformed fraction.

For determination of E_A^1 (peak positions) dilatometric curves at six different temperatures could be used. However, for determination of E_A^2 (inflection points) only the four different curves above 210 °C could be used because for the others the aging times were

not long enough for deducing the inflection points. Because of that, the uncertainty of $E_{A,i}$ is higher than that of $E_{A,p}$.

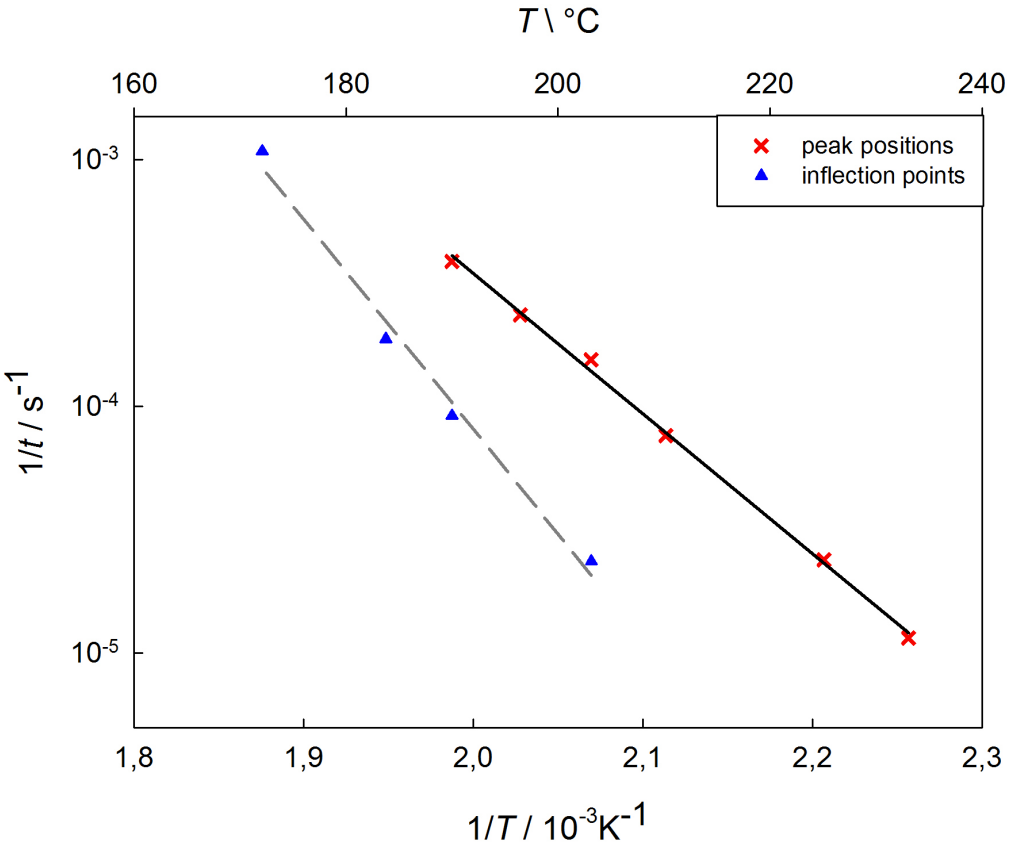

Figure 5.6: Arrhenius plot of peak positions and inflection points of isothermal dilatometric curves of Fig. 4.5. Both data sets have been fitted linearly, the fit curves are shown in black (peak positions) and grey (inflection points).

5.2.5 Time-Temperature-Precipitation Diagram

The present dilatometry studies also provide information that could be used to complement the existing TTP-diagrams. For this purpose the peak position can be correlated to the highest amount of β''. A rough estimation is also included for the onset of the plateau which follows the $\Delta L/L_0$ decrease . This onset is correlated to the highest amount of β', which is stable for temperatures lower than 260 °C.

To complete the TTP diagram, additional data was extracted from literature (see Tab. 5.1). To provide readability, the references were not directly included in the diagram, but the used data are listed in Tab. 5.3.

Only such literature data were included which refer to comparable alloy and a similar heat treatment.

In Fig. 5.7 the crosses represents points extracted from the experimental data of the present work, the dots correspond to data extracted from literature. The colouring were then inserted to fit the data. By doing that, it turned out that all literature data as well as the data obtained in this work coincide very good.

The different colour gradients were chosen in order to better visualize the observation that all metastable phases are continuously transforming into each other. Each colour thereby represents one phase in the precipitation sequence, which has been described in Sec. 5.1.

- white (low temperature and early times): Si- and Mg- single solute cluster
- dark grey: Co-cluster and transformation into pre-β''-phase
- green: pre-β'' phase
- yellow: β''-phase, all crosses laying on the pure yellow regime correspond to the peak length change positions (maximum in β'').
- orange: β'-phase, crosses laying on the pure yellow regime correspond to the beginning of the plateau (maximum amount of β').
- grey: transformation into β, at high temperature direct precipitation of β was reported.

Table 5.3: Data used for the TTP-diagram in Fig. 5.7, that has been extracted from literature. Each dot in the diagram correlates to one row of the table.

T / °C	t / s	Phase	Reference
20	600000	Co-cluster	Torsæter et al.[25]
70	1200	pre-β''	Matsuda et al.[17]
70	60000	Co-cluster	Murayama and Hono[26]
70	6000000	pre-β''	Matsuda et al.[17]
100	60000	Co-cluster	Torsæter et al.[25]
150	600000	pre-β'' and β''	Matsuda et al.[17]
175	32400	β''	Murayama et al.[34]
180	300	3 types of co-cluster	Fallah et al.[28]
180	900	2 types of co-cluster	Fallah et al.[28]
180	1200	1 type of co-cluster and pre-β''	Fallah et al.[28]
185	18000	β''	Andersen et al.[35]
250	600	8% β'' , 72% β' , 17% U2	Marioara et al.[41]
250	3600	2 phases, β' and one other.	Murayama et al.[34]
250	11000	β'	Marioara et al.[41]
250	12000	β'	Matsuda et al.[42]
350	7200	β	Murayama et al.[34]

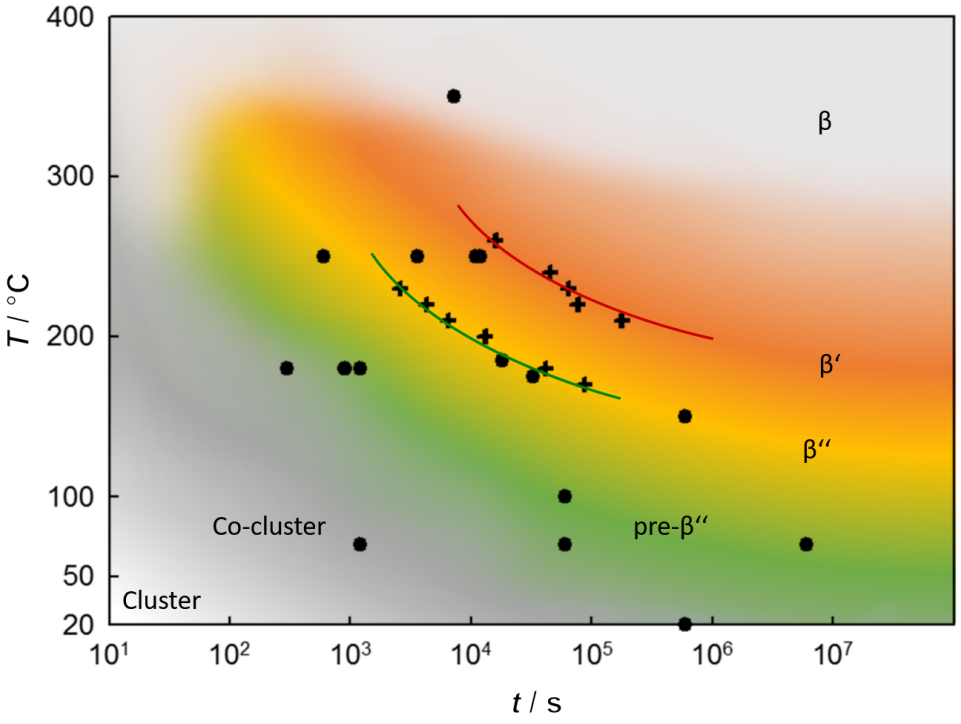

Figure 5.7: Time-temperature-precipitation diagram obtained for AW-6060 by combining the presented experimental data (cross) and those from literature (dots). The data points connected by the green line refer to the peak positions of the dilatometric curves, the red line to the plateau following the length decrease. green... pre-β'' , yellow...β'' , orange... β'

5.3 Dissolution Kinetics

Before the experimental data obtained for dissolution of the precipitates upon solution annealing will be discussed a short review of the available literature is presented.

However it appeared that there are not many articles on this topic. If at all the dissolution of the equilibrium phase $\beta\,(Mg_2Si)$ was experimentally observed[65] or numerically simulated[66].

Reiso et al.[65] investigated the microstructure during annealing by electrical resistivity measurements. The heat treatment, however, was done at very high annealing temperatures (590°C) but nonetheless it was observed that this process is diffusion controlled thereby needs time for complete dissolution.[65]

Numerical analysis was, for instance, done by Vermolen and Vuik[66], whose model included the volume fraction and the concentration of alloying elements, the matrix homogeneity and the size distribution. The impact of heating rate and temperature as a function of time was investigated. During heating with a rate of 5 K/min, dissolution already starts before the annealing temperature is reached.

Combining the information extracted from literature, one would expect, that detection of the dissolution process in a isothermal high-precision dilatometer is possible. The results of the conducted experiments have already been presented in Sec. 4.2.4. However, as already discussed there neither the total length change nor the trend of the curves provide reliable and reproducible data (see Fig. 4.8 and Fig. 4.9).

Yet, one aspect was left out in Sec. 4.2.4. The length decrease measured during annealing never reaches a comparable value to the length increase during previous aging. This applies to the second set of measurements, Fig. 4.8, as well as to the third one, Fig. 4.9. Thus, the question raised if the heating rate is too slow to suppress dissolution till isothermal condition is reached?

Each measurement sequence started with heating to solution annealing temperature with a heating rate of 100 °C/min. This heating process was included in the data files, but it was never intended to use it for analysis. However, they can now be used to identify any (potential) ongoing dissolution process during heating.

For this purpose, the length response upon heating was differentiated with respect to the temperature which results in the thermal expansion coefficient. The contribution of the thermal expansion of the matrix could not be removed, as no reference measurements

were done. The resulting change in thermal expansion coefficient is seen in Fig. 5.8. Three different measurements were included.

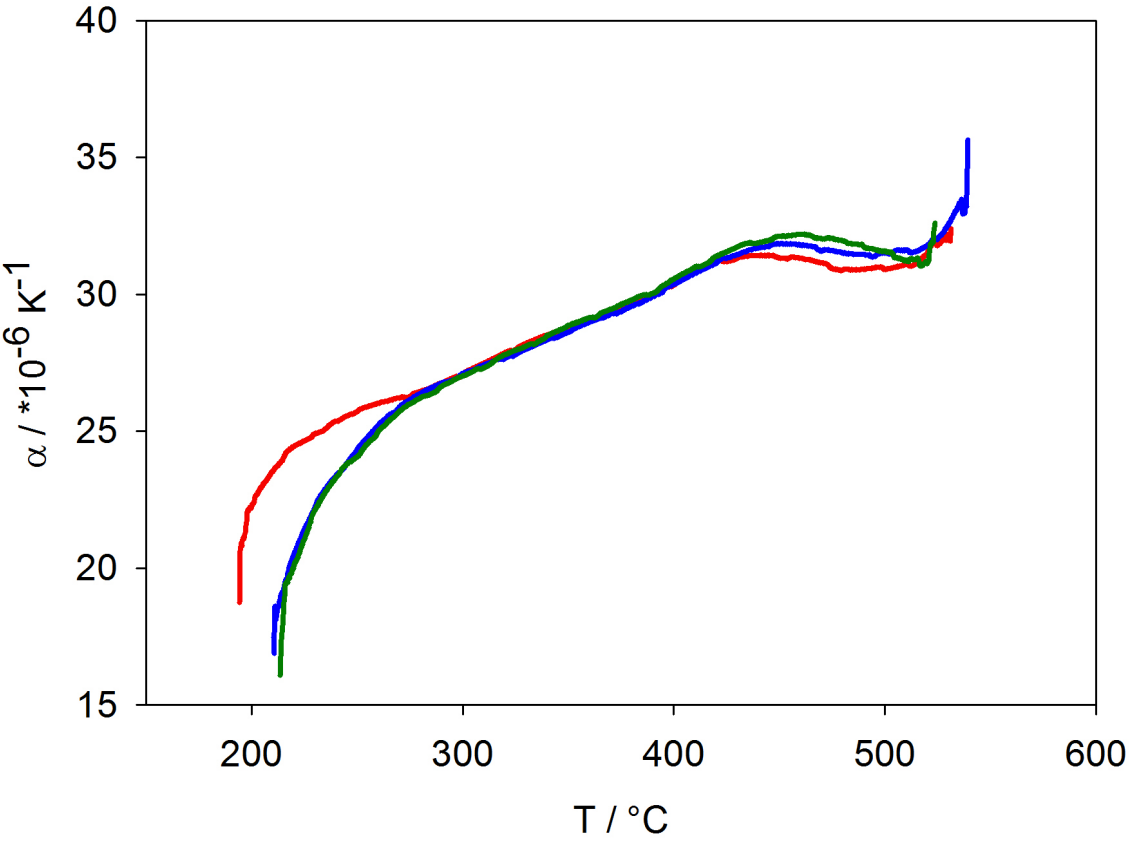

Figure 5.8: Thermal expansion coefficient derived from the length response upon heating up to the temperature of solution annealing.
red: M16 after 66 000 s at 180 °C, blue: M28 after 14 400 s at 210 °C and green: M17 after 6 000 s at 210 °C

The first fast increase is due to the lag between the measured temperature on the sample-surface and the length response of the whole specimen. Afterwards, the increase is rather linear, which is expected for an aluminium alloy in this temperature range. But when reaching approx. 450 °C, an evident decrease is observed. This clearly indicates that some microstructural changes must take place.

Milkereit et al.[8] did comparable measurements for other Al-alloys (AA7349 and AA2219), also with dilatometry. Instead of isothermal heat treatments, they performed non-isothermal cooling and reheating experiments at different cooling/heating rates. One heat treatment procedure among them was first cooling from solution annealing and afterwards reheating. For analysis, a base line was subtracted and the derivation of the length response with respect to the temperature was plotted. Depending on

the alloying element, the length response upon precipitate formation or dissolution may be different, a general statement on the direction of the response cannot be made, according to Milkereit et al.[8]. For AA7349 reheating showed first a decrease of α and afterwards an increase (already excluding the thermal expansion of the lattice). A decrease of α thereby corresponds to a length decrease. One plot from that article is reprinted in Fig. 5.9 whereby reheating with a rate of 10 K/s is shown after cooling with rates of 0.01 K/s, 1 K/s and 100 K/s. Cooling from solution annealing temperature with a low rate of 0.01 K/s cause precipitate formation already during cooling. On the contrary, a fast cooling rate of 100 K/s suppress all precipitation mechanism and precipitates are formed not before reheating. This formation process is seen in the reheating curve (Fig. 5.9) by a reduction of the signal. All three reheating curves show an increase around 400 °C, which was correlated to the dissolution of precipitates.

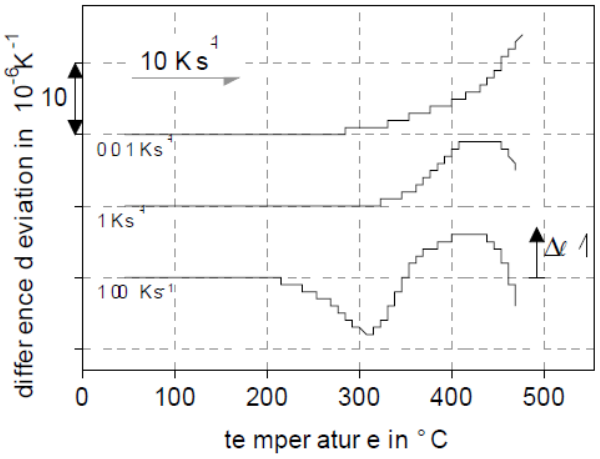

Figure 5.9: Plot reprinted from Milkereit et al.[8]. Non-isothermal dilatometric response upon reheating with a rate of 10 K/s after cooling with a rate of 0.01 K/s, 1 K/s and 100 K/s from solution annealing temperature. A base line was subtracted to exclude the thermal expansion of the lattice.

The reheating response can be quite well compared to the data obtained in the present work (Fig. 5.8). It is known from literature[67], that the coefficient of thermal expansion of aluminium approx. rises linearly with increasing temperature. Although no base line could be subtracted from the measurements, two deviations from a linear increase can be identified in Fig. 5.8. The first one between 200 °C and 300 °C is due to the difference between the temperature on the surface and the length response of the whole sample. The second one occurs between 400 °C and 500 °C. Considering the statement by Milkereit et al.[8], that the direction of the length change upon dissolution depends on the exact alloy, Fig. 5.8 and Fig. 5.9 can be correlated. The reduction or flattening of the thermal expansion coefficient, which is seen in Fig. 5.8, can be attributed to a dissolution process similar to the interpretation of Fig. 5.9.

For AW-6060 the direction of the change of the thermal expansion coefficient indicates that the volume taken by the solid solution is smaller than that taken by the combination of precipitate and matrix.

6 Conclusion

High-precision real-time dilatometry was conducted to analyze the precipitation mechanisms underlying the hardening processes of the commercial aluminium alloy AW-6060. The dilatometer is designed for isothermal heat treatments and capable of detecting absolute length changes in the range of several nanometers. This made it perfectly suitable for investigation of a low-alloyed, Al-Mg-Si alloy with a Mg/Si ratio of 1.6 as this class of alloys is known to show very little response in conventional experimental techniques as DSC. Several specimens were investigated in-situ during isothermally aging at various temperature from natural aging at 30 °C to artificial aging at 260 °C. Those measurements revealed that each of the consecutive precipitates in the aging sequence causes a change in the sign of the volume change, starting with a length increase with respect to the super-saturated solid solution followed by a decrease.

After each aging process the dissolution of the formed precipitates was also measured. The length response was complemented by hardness tests as well as XRD measurements, the latter to measure the change in lattice spacing during precipitation, and hardness tests.

Combined with a diligent literature review and a theoretical estimation of the volume changes caused by the various precipitates, it was possible to provide a complete description of the precipitation sequence, including the transition kinetics.

- *(Co-)Cluster:* The agglomeration of solute atoms was not detectable in dilatometry, but literature research reveal that separate Mg and Si cluster form which than aggregate to different types of co-clusters, which are partly Mg-rich.

- *pre-β'' -phase:* This phase marks the transition state between clusters and β'', but already has a distinct crystal structure.

- *β'' -phase:* The length increase is due to formation of β''-phase which coincides with theoretical estimations. In the peak aged condition β'' and β' are coexisting. The maximal length increase was detected at 170 °C after 80 000 s, at 260 °C no length increase was detected at all.

- β' , *U2 -phase:* According to literature, no other phases (like B' or U1) are coexisting in this regime in a balanced alloy. Regarding the volume estimations U2 also causes a length increase, β' however a significant length decrease. This decrease was also detected with dilatometry, whereby the calculated and measured length change correlated well. It was also revealed that β' is already forming at 180 °C, and at temperatures higher than 210 °C up to 260 °C β' is stable for long aging.

- β *-phase:* Calculation estimate a volume increase of 28.5×10^{-5}. This equilibrium phase could not be detected experimentally.

By extracting the peak positions from the dilatometric curves, the apparent activation energy was determined to be (109 ± 7) kJ/mol. These positions, as the region of maximum amount of β'' , as well as the plateau following the length decrease (region of maximum amount of β') have been used to complement the Time-Temperature-Precipitation diagram.

For further studies, the dilatometric setup for one specific temperature, sample and specimen holder might be optimized so that the length response also seconds after reaching the isothermal temperature can be taken into account for analysis. This could yield additional information on cluster formation or vacancy annihilation.

Appendix

SEM-images

For analyzing the influence of the argon flow controller, which has been installed within the scope of this thesis, two specimens were investigated with a scanning electron microscope (SEM). One sample (specimen number 1) was heat treated in the dilatometer before the modification was applied, the other one (specimen number 3) afterwards. In Fig. 6.1 two SEM images of sample 1, which was assumed to have a pronounced oxide layer, are seen. The right one represents a typical aluminium oxide surface in BSE (backscattered electron) imaging mode, which was taken on the side wall of the sample. The left one shows a topview of cylindrical sample in SE (secondary electron) mode. The sample is located in the upper half of the image. An oxide layer thickness of several μm (approx. 3-5 μm) was estimated. In Fig. 6.2 an EDX (energy-dispersive x-ray spectroscopy) spectrum of the oxide layer is seen. A few EDX spectra were taken, but only one is shown as an example. The oxygen in the oxide layer was clearly identified.

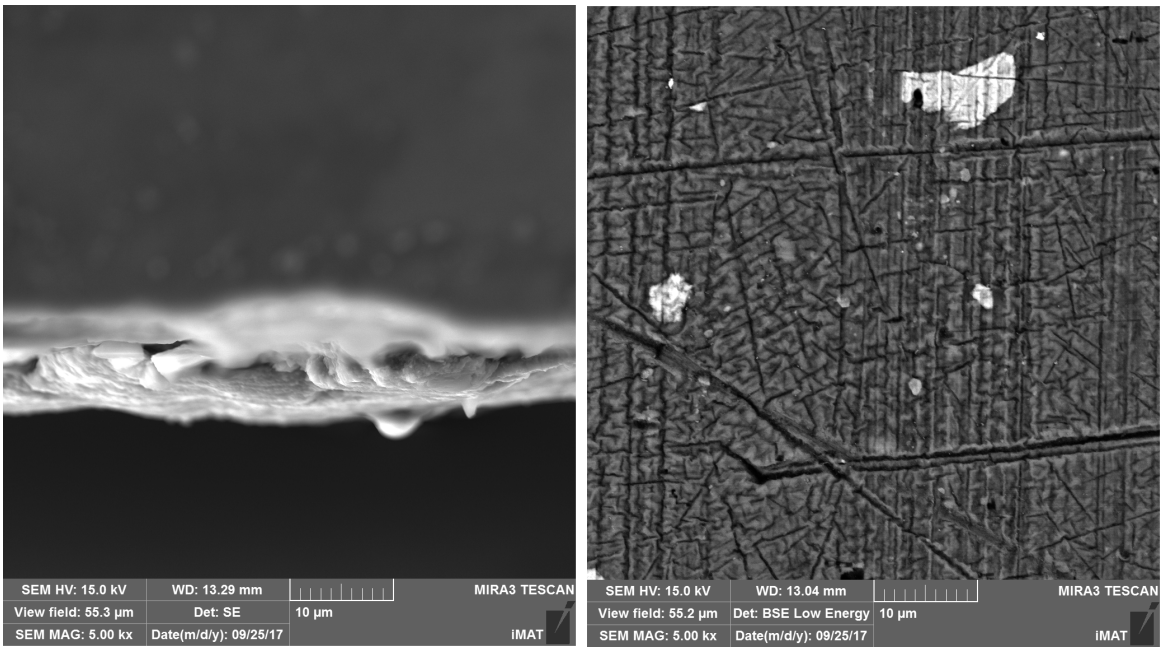

Figure 6.1: Two SEM-images of the oxidized specimen
Left: topview of the sample in SE-mode. Right: surface on the side wall in BSE-mode

EDAX TEAM

Page2

EDS Spot 1

kV:	15	Mag:14682	Takeoff: 31.1	Live Time(s): 50	Amp Time(µs):1.92	Resolution:(eV)129.3

EDS Spot 1 - Det 1

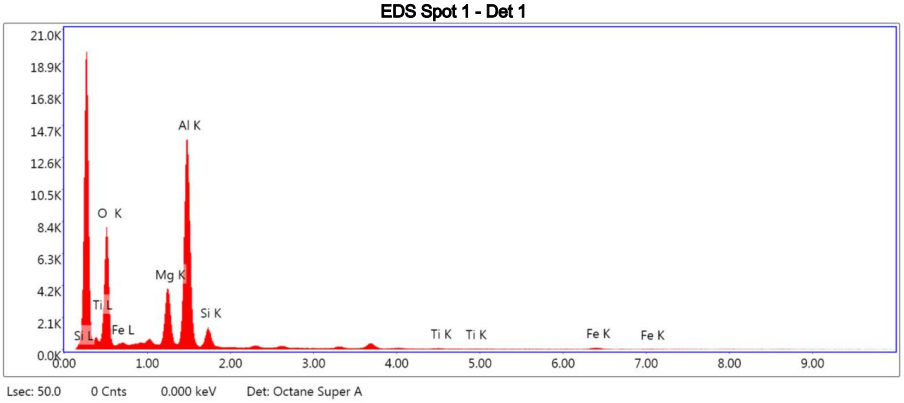

Lsec: 50.0 0 Cnts 0.000 keV Det: Octane Super A

eZAF Smart Quant Results

Element	Weight %	Atomic %	Net Int.	Error %	Kratio	Z	A	F
O K	34.24	46.81	1012.23	7.62	0.1612	1.0793	0.4361	1.0000
MgK	12.23	11.00	666.57	4.62	0.0898	0.9908	0.7371	1.0057
AlK	45.49	36.87	2302.67	4.32	0.3170	0.9529	0.7305	1.0013
SiK	5.57	4.33	211.61	7.76	0.0304	0.9726	0.5608	1.0008
TiK	0.35	0.16	7.48	37.16	0.0029	0.8241	0.9788	1.0340
FeK	2.12	0.83	24.08	14.82	0.0183	0.8038	1.0022	1.0708

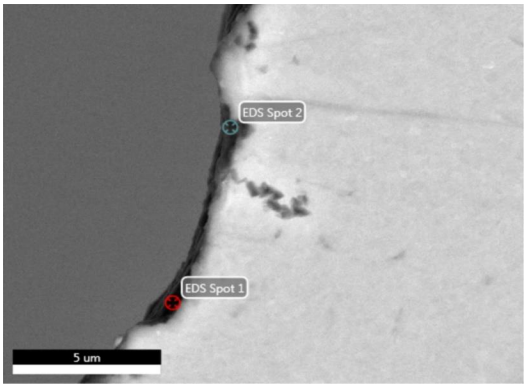

Figure 6.2: EDX spectra of the oxide layer. On the image, a topview of the sample is seen.

In Fig. 6.3 pictures of the sample after heat treatment under argon atmosphere are shown. The left images is a SE, the right a BSE image of the same surface area on the side wall. The typical characteristics of an oxide layer (see Fig. 6.1) are not visible. No oxide was found on the surface with EDX, which is seen in Fig. 6.4. Also here, only one EDX spectrum is shown as an example.

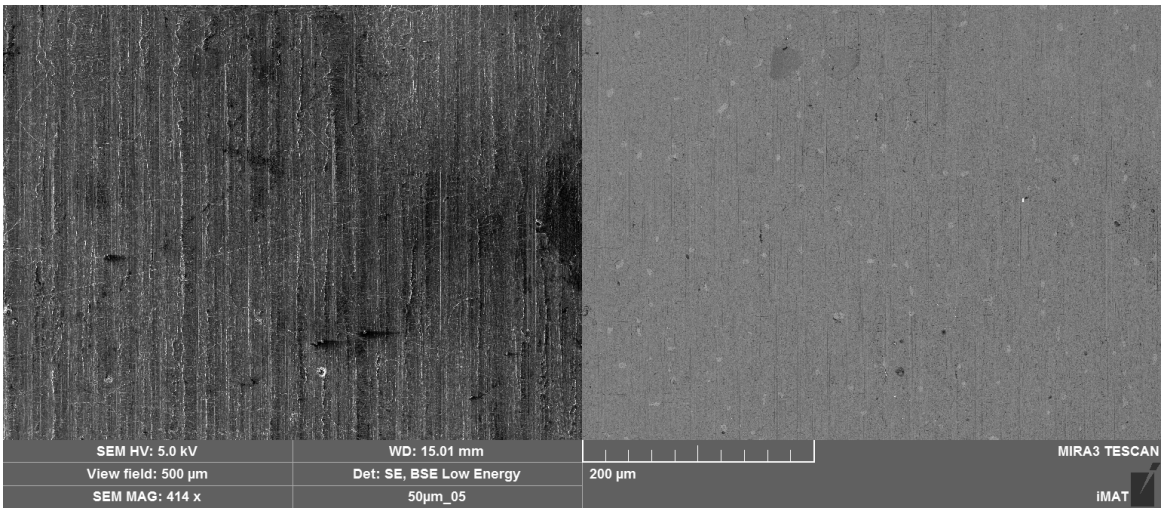

Figure 6.3: SEM image in SE (left) and BSE (right) mode of the side wall of sample 3.

EDAX TEAM

Page3

EDS Spot 2

kV:	15	Mag:19380	Takeoff: 35.1	Live Time(s): 45.8	Amp Time(µs):1.92	Resolution:(eV)129.3

EDS Spot 2 - Det 1

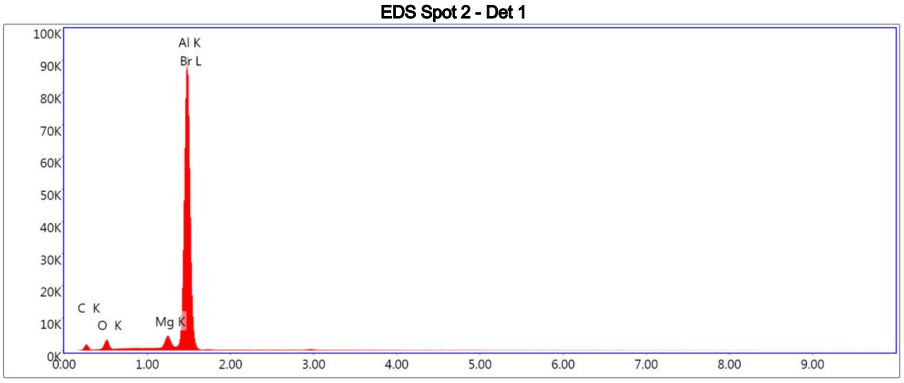

Lsec: 45.8 0 Cnts 0.000 keV Det: Octane Super A

eZAF Smart Quant Results

Element	Weight %	Atomic %	Net Int.	Error %	Kratio	Z	A	F
C K	14.05	29.35	207.26	11.65	0.0181	1.1946	0.1077	1.0000
O K	6.80	10.66	479.83	9.36	0.0207	1.1409	0.2670	1.0000
MgK	3.05	3.14	722.03	3.57	0.0271	1.0506	0.8418	1.0078
BrL	22.59	7.09	2860.38	2.46	0.1942	0.7929	1.0840	1.0001
AlK	53.51	49.75	12386.35	2.62	0.4773	1.0110	0.8818	1.0005

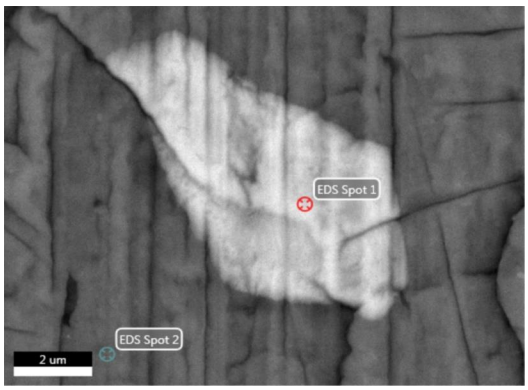

Figure 6.4: EDX spectra of the surface of sample 3. The image was taken at the side wall of the sample.

X-ray fluoresence spectroscopy

13-Dec-2017 14:44:36 **Results for <Omnian>** Page 1

Nr	Ident	Seq	Time	Pos	Norm F	Mg C	Mg Unit	Al C	Al Unit	Si C
1	EH_Glas_brownish	1/1	13-Dec-2017 12:57:18	Lge	1.855	36.058	%	3.016	%	59.314
2	EH_glas_brownish_outside	1/1	13-Dec-2017 13:21:48	Lge	2.242	5.585	%	3.572	%	88.376
3	EH_Glas_white_outside	1/1	13-Dec-2017 13:59:55	Lge	1.687	2.253	%	4.019	%	92.922
4	EH_?las_????????????????	Ave/3	13-Dec-2017 13:59:55	Lge	1.928	14.632	%	3.535	%	80.204
5	EH_?las_????????????????	SDev/3	13-Dec-2017 13:59:55	Lge	0.285	18.630	%	0.503	%	18.233

Nr	Si Unit	P C	P Unit	Cl C	Cl Unit	K C	K Unit	Ca C	Ca Unit	Ti C	Ti Unit	Fe C	Fe Unit	Cu C	Cu Unit	Sr C	Sr Unit
1	%	0.605	%	0.652	%	0.071	%	0.183	%	0.019	%	0.036	%	0.002	%	0.002	%
2	%	0.842	%	1.025	%	0.142	%	0.257	%	0.031	%	0.052	%	0.002	%	0.004	%
3	%	0.080	%	0.400	%	0.122	%	0.038	%	0.023	%	0.040	%	0.003	%	0.003	%
4	%	0.509	%	0.693	%	0.112	%	0.159	%	0.025	%	0.043	%	0.002	%	0.003	%
5	%	0.3901	%	0.314	%	0.037	%	0.112	%	0.006	%	0.008	%	0.0005	%	0.0007	%

Nr	Zr C	Zr Unit	Mn C	Mn Unit	Eu C	Eu Unit	Gd C	Gd Unit	S C	S Unit	Sc C	Sc Unit	Sn C	Sn Unit
1	0.042	%												
2	0.071	%	0.000	%	0.015	%	0.027	%						
3	0.063	%	0.004	%					0.022	%	0.002	%	0.006	%
4	0.058	%	0.002	%	0.015	%	0.027	%	0.022	%	0.002	%	0.006	%
5	0.015	%	0.003	%	No intensity		No intensity		No intensity		No intensity		No intensity	

Figure 6.5: XFS measurements of the fused silica specimen holder. The relevant information is highlighted by the yellow rectangle and the concentration of magnesium was additionally framed in red.

After installing the argon flow controller, which enabled an argon atmosphere in the dilatometer, the specimen holder (fused silica tube) was vaporized with a brownish layer after several measurements sequences. For analysis of this layer XRS analysis was performed. In Fig. 6.5, three measurements are seen (yellow frame). The first one was done on the inside of the specimen holder, the second on at the same spot but from the outside and the last one on a non-vaporized spot on the specimen holder. The difference in magnesium-concentration (red frame) clearly indicated that magnesium is evaporating from the sample during heat treatment.

Bibliography

[1] M. I. Daoudi, A. Triki and A. Redjaimia. DSC study of the kinetic parameters of the metastable phases formation during non-isothermal annealing of an Al-Si-Mg alloy. *Journal of Thermal Analysis and Calorimetry*, **104** (2011) 627.
DOI: 10.1007/s10973-010-1099-8.

[2] A. Hayoune and D. Hamana. Structural evolution during non-isothermal ageing of a dilute al-Cu alloy by dilatometric analysis. *Journal of Alloys and Compounds*, **474** (2009) 118.
DOI: 10.1016/j.jallcom.2008.06.070.

[3] D. Hamana, L. Baziz and M. Bouchear. Kinetics and mechanism of formation and transformation of metastable β'-phase in Al-Mg alloys. *Materials Chemistry and Physics*, **84** (2004) 112.
DOI: 10.1016/j.matchemphys.2003.11.001.

[4] G. Edwards, K. Stiller, G. Dunlop and M. Couper. The precipitation sequence in Al-Mg-Si alloys. *Acta Materialia*, **46** (1998) 3893.
DOI: 10.1016/S1359-6454(98)00059-7.

[5] C. Ravi and C. Wolverton. First-principles study of crystal structure and stability of Al-Mg-Si -(Cu) precipitates. *Acta Materialia*, **52** (2004) 4213.
DOI: 10.1016/j.actamat.2004.05.037.

[6] M. Zandbergen, Q. Xu, A. Cerezo and G. Smith. Study of precipitation in Al-Mg-Si alloys by Atom Probe Tomography I. Microstructural changes as a function of ageing temperature. *Acta Materialia*, **101** (2015) 136.
DOI: 10.1016/j.actamat.2015.08.017.

[7] B. Milkereit, N. Wanderka, C. Schick and O. Kessler. Continuous cooling precipitation diagrams of Al-Mg-Si alloys. *Materials Science and Engineering: A*, **550** (2012) 87.
DOI: 10.1016/j.msea.2012.04.033.

[8] B. Milkereit, M. Reich and O. Kessler. Detection of Quench Induced Precipitation in Al Alloys by Dilatometry. *Materials Science Forum*, **877** (2017) 147.

[9] M. Luckabauer, W. Sprengel and R. Würschum. A high-stability non-contact dilatometer for low-amplitude temperature-modulated measurements. *Review of Scientific Instruments*, **87** (2016) 075116.
DOI: 10.1063/1.4959200.

[10] D. Porter and K. Easterling. *Phase Transformations in Metals and Alloys*. Chapman & Hall, 2. edition (1992).

[11] G. Gottstein. *Materialwissenschaft und Werkstofftechnik*. Springer-Verlag, 4. edition (2014).

[12] B. Milkereit, L. Giersberg, O. Kessler and C. Schick. Isothermal Time-Temperature-Precipitation Diagram for an Aluminum Alloy 6005A by In Situ DSC Experiments. *Materials*, **7** (2014) 2631.
DOI: 10.3390/ma7042631.

[13] F. Ostermann. *Anwendungstechnologie Aluminium*. Springer Vieweg, Berlin, Heidelberg, 3. edition (2015).
DOI: 10.1007/978-3-662-43807-7.

[14] G. D. Preston. Structure of Age-Hardened Aluminium-Copper Alloys. *Nature*, (1938).
DOI: 10.1038/142570a0.

[15] L. Spiess, G. Teichert, R. Schwarzer, H. Behnken and C. Genzel. *Moderne Röntgenbeugung*. Viewweg+Teubner, 2. edition (2009).

[16] W. Seidel. *Werkstofftechnik*. Carl Hanser Verlag (1999).

[17] K. Matsuda, S. Ikeno, H. Gamada, K. Fujii, Y. Uetani, T. Sato and A. Kamio. High-Resolution Electron Microscopy on the Structure of Guinier-Preston Zones in an Al-1.6 mass pct Mg_2Si alloy. *Metallurgical and Materials Transactions A*, **29** (1998) 1161.
DOI: 10.1007/s11661-998-0242-7.

[18] L. Zhen, W. D. Fei, S. B. Kang and H. W. Kim. Precipitation behaviour of Al-Mg-Si alloys with high silicon content. *Journal of Materials Science*, **32** (1997) 1895.
DOI: 10.1023/A:1018569226499.

[19] C. Marioara, S. Andersen, J. Jansen and H. Zandbergen. Atomic model for GP-zones in a 6082 Al-Mg-Si system. *Acta Materialia*, **49** (2001) 321. DOI: 10.1016/S1359-6454(00)00302-5.

[20] C. D. Marioara, S. J. Andersen, H. W. Zandbergen and R. Holmestad. The influence of alloy composition on precipitates of the Al-Mg-Si system. *Metallurgical and Materials Transactions A*, **36** (2005) 691. DOI: 10.1007/s11661-005-0185-1.

[21] P. H. Ninive, A. Strandlie, S. Gulbrandsen-Dahl, W. Lefebvre, C. D. Marioara, S. J. Andersen, J. Friis, R. Holmestad and O. M. Løvvik. Detailed atomistic insight into the β'' phase in Al-Mg-Si alloys. *Acta Materialia*, **69** (2014) 126. DOI: 10.1016/j.actamat.2014.01.052.

[22] M. Murayama, K. Hono, M. Saga and M. Kikuchi. Atom probe studies on the early stages of precipitation in Al-Mg-Si alloys. *Materials Science and Engineering: A*, **250** (1998) 127. DOI: 10.1016/S0921-5093(98)00548-6.

[23] M. Liu, J. Čížek, C. S. Chang and J. Banhart. Early stages of solute clustering in an Al-Mg-Si alloy. *Acta Materialia*, **91** (2015) 355. DOI: 10.1016/j.actamat.2015.02.019.

[24] M. van Huis, J. Chen, M. Sluiter and H. Zandbergen. Phase stability and structural features of matrix-embedded hardening precipitates in Al-Mg-Si alloys in the early stages of evolution. *Acta Materialia*, **55** (2007) 2183. DOI: 10.1016/j.actamat.2006.11.019.

[25] M. Torsæter, H. S. Hasting, W. Lefebvre, C. D. Marioara, J. C. Walmsley, S. J. Andersen and R. Holmestad. The influence of composition and natural aging on clustering during preaging in Al-Mg-Si alloys. *Journal of Applied Physics*, **108** (2010) 073527. DOI: 10.1063/1.3481090.

[26] M. Murayama and K. Hono. Pre-precipitate clusters and precipitation processes in Al-Mg-Si alloys. *Acta Materialia*, **47** (1999) 1537. DOI: 10.1016/S1359-6454(99)00033-6.

[27] V. Fallah, B. Langelier, N. Ofori-Opoku, B. Raeisinia, N. Provatas and S. Esmaeili. Cluster evolution mechanisms during aging in Al-Mg-Si alloys.

Acta Materialia, **103** (2016) 290.
DOI: 10.1016/j.actamat.2015.09.027.

[28] V. Fallah, A. Korinek, N. Ofori-Opoku, B. Raeisinia, M. Gallerneault, N. Provatas and S. Esmaeili. Atomic-scale pathway of early-stage precipitation in Al-Mg-Si alloys. *Acta Materialia*, **82** (2015) 457.
DOI: 10.1016/j.actamat.2014.09.004.

[29] M. Werinos, H. Antrekowitsch, T. Ebner, R. Prillhofer, P. Uggowitzer and S. Pogatscher. Hardening of Al-Mg-Si alloys: Effect of trace elements and prolonged natural aging. *Materials & Design*, **107** (2016) 257.
DOI: 10.1016/j.matdes.2016.06.014.

[30] H. Seyedrezai, D. Grebennikov, P. Mascher and H. S. Zurob. Study of the early stages of clustering in Al-Mg-Si alloys using the electrical resistivity measurements. *Materials Science and Engineering: A*, **525** (2009) 186.
DOI: 10.1016/j.msea.2009.06.054.

[31] V. N. Grau, A. Cuniberti, A. Tolley, V. C. Riglos and M. Stipcich. Solute clustering behavior between 293K and 373K in a 6082 Aluminum alloy. *Journal of Alloys and Compounds*, **684** (2016) 481.
DOI: 10.1016/j.jallcom.2016.05.197.

[32] K. Matsuda, T. Naoi, K. Fujii, Y. Uetani, T. Sato, A. Kamio and S. Ikeno. Crystal structure of the β'' phase in an Al-l.0mass%Mg_2Si-0.4mass%Si alloy. *Materials Science and Engineering: A*, **262** (1999) 232.
DOI: 10.1016/S0921-5093(98)00962-9.

[33] Q. Du, K. Tang, C. D. Marioara, S. J. Andersen, B. Holmedal and R. Holmestad. Modeling over-ageing in Al-Mg-Si alloys by a multi-phase CALPHAD-coupled Kampmann-Wagner Numerical model. *Acta Materialia*, **122** (2017) Supplement C 178.
DOI: 10.1016/j.actamat.2016.09.052.

[34] N. Murayama, R. Uemori, N. Hashimoto, M. Saga and M. Kikuchi. Effect of silicon addition on the composition and structure of fine-scale precipitates in Al-Mg-Si alloys. *Scripta Materialia*, **36** (1997) 89.
DOI: 10.1016/S1359-6462(96)00358-2.

[35] S. Andersen, H. Zandbergen, J. Jansen, C. Træholt, U. Tundal and O. Reiso. The crystal structure of the β'' phase in Al-Mg-Si alloys. *Acta*

Materialia, **46** (1998) 3283.
DOI: 10.1016/S1359-6454(97)00493-X.

[36] H. S. Hasting, A. G. Frøseth, S. J. Andersen, R. Vissers, J. C. Walmsley, C. D. Marioara, F. Danoix, W. Lefebvre and R. Holmestad. Composition of β'' precipitates in Al-Mg-Si alloys by atom probe tomography and first principles calculations. *Journal of Applied Physics*, **106** (2009) 123527.
DOI: 10.1063/1.3269714.

[37] K. Momma and F. Izumi. VESTA3 for three-dimensional visualization of crystal, volumetric and morphology data. *Journal of Applied Crystallography*, **44** (2011) 1272.
DOI: 10.1107/S0021889811038970.

[38] F. Ehlers, S. Dumoulin and R. Holmestad. 3D modelling of β'' in Al-Mg-Si: Towards an atomistic level ab initio based examination of a full precipitate enclosed in a host lattice. *Computational Materials Science*, **91** (2014) 200.
DOI: 10.1016/j.commatsci.2014.04.060.

[39] C.-S. Tsao, C.-Y. Chen, U.-S. Jeng and T.-Y. Kuo. Precipitation kinetics and transformation of metastable phases in Al-Mg-Si alloys. *Acta Materialia*, **54** (2006) 4621.
DOI: 10.1016/j.actamat.2006.06.005.

[40] S. Andersen, C. Marioara, A. Frøseth, R. Vissers and H. Zandbergen. Crystal structure of the orthorhombic U2-$Al_4Mg_4Si_4$ precipitate in the Al-Mg-Si alloy system and its relation to the β' and β'' phases. *Materials Science and Engineering: A*, **390** (2005) 127.
DOI: 10.1016/j.msea.2004.09.019.

[41] C. D. Marioara, H. Nordmark, S. J. Andersen and R. Holmestad. Post-β'' phases and their influence on microstructure and hardness in 6xxx Al-Mg-Si alloys. *Journal of Materials Science*, **41** (2006) 471.
DOI: 10.1007/s10853-005-2470-1.

[42] K. Matsuda, Y. Sakaguchi, Y. Miyata, Y. Uetani, T. Sato, A. Kamio and S. Ikeno. Precipitation sequence of various kinds of metastable phases in Al-1.0mass % Mg_2Si-0.4mass% Si alloy. *Journal of Materials Science*, **35** (2000) 179.
DOI: 10.1023/A:1004769305736.

[43] K. Matsuda, S. Ikeno, K. Terayama, H. Matsui, T. Sato and Y. Uetani. Comparison of Precipitates between Excess Si-Type and Balanced-Type Al-Mg-Si alloys during Continuous Heating. *Metallurgical and Materials Transactions A*, **36** (2005) 2007.
DOI: 10.1007/s11661-005-0321-y.

[44] M. H. Jacobs. The structure of the metastable precipitates formed during ageing of an Al-Mg-Si alloy. *The Philosophical Magazine: A Journal of Theoretical Experimental and Applied Physics*, **26** (1972) 1.
DOI: 10.1080/14786437208221015.

[45] S. Andersen, C. Marioara, R. Vissers, A. Frøseth and H. Zandbergen. The structural relation between precipitates in Al-Mg-Si alloys, the Al-matrix and diamond silicon, with emphasis on the trigonal phase U1-$MgAl_2Si_2$. *Materials Science and Engineering: A*, **444** (2007) 157.
DOI: 10.1016/j.msea.2006.08.084.

[46] K. Matsuda, S. Tada, S. Ikeno, T. Sato and A. Kamio. Crystal system of rod-shaped precipitates in an Al-1.0mass% Mg_2Si-0.4mass % Si alloy. *Scripta Metallurgica et Materialia*, **32** (1995).
DOI: 10.1016/0956-716X(95)00121-B.

[47] K. Matsuda, S. Ikeno, T. Sato and A. Kamio. A metastable phase having the orthorhombic crystal lattice in an Al-1.0mass% Mg_2Si - 0.4mass%Si alloy. *Scripta Materialia*, **34** (1996).
DOI: 10.1016/1359-6462(96)00057-7.

[48] A. H. Geisler and J. K. Hill. Analyses and interpretations of X-ray diffraction effects in patterns of aged alloys. *Acta Crystallographica*, **1** (1948) 238.
DOI: 10.1107/S0365110X48000661.

[49] A. Gupta, D. Lloyd and S. Court. Precipitation hardening in Al-Mg-Si alloys with and without excess Si. *Materials Science and Engineering: A*, **316** (2001) 11.
DOI: 10.1016/S0921-5093(01)01247-3.

[50] A. Serizawa, S. Hirosawa and T. Sato. Three-Dimensional Atom Probe Characterization of Nanoclusters Responsible for Multistep Aging Behavior of an Al-Mg-Si Alloy. *Metallurgical and Materials Transactions A*, **39** (2008) 243.
DOI: 10.1007/s11661-007-9438-5.

[51] M. van Huis, J. Chen, H. Zandbergen and M. Sluiter. Phase stability and structural relations of nanometer-sized, matrix-embedded precipitate phases in Al-Mg-Si alloys in the late stages of evolution. *Acta Materialia*, **54** (2006) 2945. DOI: 10.1016/j.actamat.2006.02.034.

[52] R. Vissers, M. van Huis, J. Jansen, H. Zandbergen, C. Marioara and S. Andersen. The crystal structure of the β' phase in Al-Mg-Si alloys. *Acta Materialia*, **55** (2007) 3815. DOI: 10.1016/j.actamat.2007.02.032.

[53] K. Matsuda, S. Tada and S. Ikeno. The morphology of precipitates in an Al-1 wt% Mg_2Si Alloy. *Journal of Electron Microscopy*, **42** (1993) 1. DOI: 10.1093/oxfordjournals.jmicro.a051001.

[54] N. Belov, D. Eskin and A. Aksenov. *Multicomponent Phase Diagrams: Applications for Commercial Aluminum Alloys*. Elsevier Science (2005). Chapter 2.4.

[55] R. Hu, T. Ogura, H. Tezuka, T. Sato and Q. Liu. Dispersoid Formation and Recrystallization Behavior in an Al-Mg-Si-Mn Alloy. *Journal of Materials Science & Technology*, **26** (2010) 237. DOI: 10.1016/S1005-0302(10)60040-0.

[56] L. Lodgaard and N. Ryum. Precipitation of dispersoids containing Mn and/or Cr in Al-Mg-Si alloys. *Materials Science and Engineering: A*, **283** (2000) 144. DOI: https://doi.org/10.1016/S0921-5093(00)00734-6.

[57] S. Ji, W. Yang, F. Gao, D. Watson and Z. Fan. Effect of iron on the microstructure and mechanical property of Al-Mg-Si-Mn and Al-Mg-Si diecast alloys. *Materials Science and Engineering: A*, **564** (2013) 130. DOI: 10.1016/j.msea.2012.11.095.

[58] G. Chiarotti. 1.6 Crystal structures and bulk lattice parameters of materials quoted in the volume. Part of Landolt-Börnstein - Group III Condensed Matter 24B (Electronic and Vibrational Properties in SpringerMaterials) (1994). DOI: 10.1007/10086058_6.

[59] S. Pramanik, J. Cherusseri, N. S. Baban, L. Sowntharya and K. K. Kar. Metal Matrix Composites: Theory, Techniques, and Applications (Composite Materials in SpringerMaterials) (2017). DOI: 10.1007/978-3-662-49514-8_11.

[60] W. Pearson. *A Handbook of lattice spacings and structures of metals and alloys*. Pergamon Press (1958).

[61] M. Takeda, F. Ohkubo, T. Shirai and K. Fukui. Stability of metastable phases and microstructures in the ageing process of Al-Mg-Si ternary alloys. *Journal of Materials Science*, **33** (1998) 2385.
DOI: 10.1023/A:1004355824857.

[62] F. Martinsen, F. Ehlers, M. Torsæter and R. Holmestad. Reversal of the negative natural aging effect in Al-Mg-Si alloys. *Acta Materialia*, **60** (2012) 6091.
DOI: 10.1016/j.actamat.2012.07.047.

[63] C. Marioara, S. Andersen, J. Jansen and H. Zandbergen. The influence of temperature and storage time at RT on nucleation of the β'' phase in a 6082 Al-Mg-Si alloy. *Acta Materialia*, **51** (2003) 789.
DOI: 10.1016/S1359-6454(02)00470-6.

[64] M. I. Daoudi, A. Triki, A. Redjaimia and C. Yamina. The determination of the activation energy varying with the precipitated fraction of β'' metastable phase in an Al-Mg-Si alloy using non-isothermal dilatometry. *Thermochimica Acta*, **577** (2014) 5.
DOI: 10.1016/j.tca.2013.12.007.

[65] O. Reiso, N. Ryum and J. Strid. Melting of secondary-phase particles in Al-Mg-Si alloys. *Metallurgical and Materials Transactions A*, **24** (1993) 12 2629.
DOI: 10.1007/BF02659487.

[66] F. Vermolen and C. Vuik. A mathematical model for the dissolution of particles in multi-component alloys. *Journal of Computational and Applied Mathematics*, **126** (2000) 233.
DOI: 10.1016/S0377-0427(99)00355-6.

[67] F. C. Nix and D. MacNair. The Thermal Expansion of Pure Metals: Copper, Gold, Aluminum, Nickel, and Iron. *Phys. Rev.*, **60** (1941) 597.
DOI: 10.1103/PhysRev.60.597.

Acknowledgment

At this point I would like to thank all who contributed to the success of this thesis.

The Austrian Economics Chamber

for awarding the fellowship for research (Forschungsstipendium). The financial support is greatly appreciated.

Univ.-Prof. Dr. Roland Würschum, Institute of Materials Physics, TU Graz

for his continuous support and supervision during the course of this thesis.

Dipl.-Ing. Robert Enzinger, Institute of Materials Physics, TU Graz

for co-supervising, for the assistance during the experimental work as well as for the numerous discussions.

Dr. Martin Luckabauer, formerly Institute of Materials Physics, TU Graz

for the support during the whole project, already starting with the supervision during the project laboratory.

Dipl. Ing. Stefan Pachmajer, Institute of Solid State Physics, TU Graz

for conducting the XRD and XRF measurements.

Assoz.Prof. Dr.mont. Stefan Pogatscher, Institute of Nonferrous Metallurgy, Montanuniversität Leoben

for enabling the photoemission spectroscopy and the simulations as well as for the valuable discussion during his visit at the Institute of Materials Physics.

Dipl. Ing. Fatemeh Iranshahi and Dipl. Ing. Ricardo Buzolin, Institute of Materials Science, Joining and Forming, TU Graz

for conducting the scanning electron microscopy (SEM) imaging.

All colleagues from the Institute of Materials Physics

for the friendly working atmosphere and their support.

Family

for their consistent support, understanding and encouragement throughout the whole time.